



Recent eruptive history and magma reservoir dynamics on the southern East Pacific Rise at 17°30'S

Eric C. Bergmanis, John Sinton, and Kenneth H. Rubin

Department of Geology and Geophysics, University of Hawaii at Manoa, 1680 East-West Road, POST615C, Honolulu, Hawaii 96822, USA (bergmani@hawaii.edu)

[1] Submersible-based geologic observations and geochemical, magnetic paleointensity, and ($^{210}\text{Pb}/^{226}\text{Ra}$) radioactive disequilibria data indicate that at least five distinct lava sequences (three normal mid-ocean ridge basalt (N-MORB) and two transitional mid-ocean ridge basalt (T-MORB)) have been erupted within the last several hundred years along a 27-km-long portion of the fast spreading East Pacific Rise near 17°30'S. Isotopic and geochemical variations, both within and between eruptive units, indicate mixing of different primary magmas concurrently with differentiation in shallow-level subaxial magma reservoirs. Differentiation trends are linked to geographical variations in axial magma chamber (AMC) characteristics, with the lowest MgO samples erupted above the shallowest portion of the AMC, suggesting that pre-eruptive magma temperature is in part controlled by the depth-dependent efficacy of hydrothermal cooling. A third-order axial discontinuity at ~17°29'S coincides with a narrowing of the subaxial melt lens and an increase in lava MgO to the south; we interpret the latter to reflect a sharp increase in the mixing proportion of recharge to low-MgO magma residing in the melt lens. Magmatic evolution of this area over the last few hundred years reflects continually evolving conditions in the subsurface and mantle melting processes that vary rapidly at rates that are at least as great as the eruption rate.

Components: 15,984 words, 10 figures, 4 tables.

Keywords: East Pacific Rise; mid-ocean ridges; magma chamber; MORB geochemistry; Magnetic paleointensity; U-series age data.

Index Terms: 3035 Marine Geology and Geophysics: Midocean ridge processes; 1036 Geochemistry: Magma chamber processes (3618); 1021 Geochemistry: Composition of the oceanic crust.

Received 6 July 2007; **Revised** 7 September 2007; **Accepted** 25 September 2007; **Published** 21 December 2007.

Bergmanis, E. C., J. Sinton, and K. H. Rubin (2007), Recent eruptive history and magma reservoir dynamics on the southern East Pacific Rise at 17°30'S, *Geochem. Geophys. Geosyst.*, 8, Q12O06, doi:10.1029/2007GC001742.

Theme: Formation and Evolution of Oceanic Crust Formed at Fast Spreading Rates

Guest Editors: D. A. H. Teagle and D. Wilson

1. Introduction

[2] The study of individual volcanic eruptions on mid-ocean ridges provides constraints on the nature and timescales of magmatic processes, including

the diversity of mantle source rocks, frequency and nature of magma recharge and eruption, and the relative roles of magma mixing and differentiation processes. The character and along-axis scale of compositional heterogeneity within and between

individual eruptions has implications for the efficacy and spatial and temporal scales of mixing in subaxial magma reservoirs, and for magma recharge events.

[3] Two aspects of the southern East Pacific Rise (SEPR) near 17°30'S make this area particularly useful for the study of lava flows at high spatial and temporal resolution. Very high spreading rate (~146 mm/a, where a is years) [Naar and Hey, 1989] corresponds with high eruption frequency of generally low-volume single eruptive episodes [Sinton et al., 2002]; thus the sampling rate of subaxial events is likely to be as high as on any submarine mid-ocean ridge on Earth. This is also a region of moderate isotopic heterogeneity [Mahoney et al., 1994; Hall et al., 2006] and variable melting produces a wide range of magma compositions that can be used to track parent melt compositions and mixing in the shallow crust. In this study we report and investigate the geographical extent of magma types and geochemical heterogeneity of several discrete eruptive units along the SEPR between 17°21'S and 17°36'S, and the implications of new age constraints for the timing of shallow-level magmatic processes to unprecedented scale. Although the data and observations presented here also have implications for understanding mantle melting in this area, a detailed analysis of those processes will be presented in a future contribution.

[4] The SEPR near 17°30'S represents a maximum in magma supply for the ~1100-km-long region extending from the Easter Microplate near 23°S to the Garrett Fracture Zone near 13°S. The ridge axis is shallowest between 17° and 17°30'S and the axial cross-sectional area is greatest near 17°30'S [Scheirer and Macdonald, 1993]. Average depth of the seismic reflector interpreted to be the top of the axial magma chamber (AMC) is shallower here than on the northern East Pacific Rise (EPR) between 9° and 10° (~1.3 km versus ~1.6 km) and is less than 1 km from the seafloor at 17°26'S [Detrick et al., 1993]. The axial mantle Bouguer anomaly reaches a regional minimum between 16° and 19°S; perhaps a result of lower-density mantle [Cormier et al., 1995].

[5] MgO contents of axial lavas from 14°30'S to 20°42'S form a broad dome centered around 16°–19°S [Sinton et al., 1991], suggesting a regional high in eruption temperature. Axial lavas from 15°48'S to 20°42'S have more radiogenic Sr, Nd and Pb isotopic compositions than ridge segments to the north and south, with $^{87}\text{Sr}/^{86}\text{Sr}$ (0.70271),

$^{206}\text{Pb}/^{204}\text{Pb}$ (18.642), and $^3\text{He}/^4\text{He}$ (10.94Ra) maxima, and ϵ_{Nd} (+8.9) and $^{21}\text{Ne}/^{22}\text{Ne}$ (0.042) minima near 17–17°30'S [Bach et al., 1994; Mahoney et al., 1994; Niu et al., 1996; Kurz et al., 2005]. The near-axis region is populated by an unusual abundance of seamounts that have greater isotopic variability than the axial lavas ($^{87}\text{Sr}/^{86}\text{Sr}$: 0.70244–0.70313, $^{206}\text{Pb}/^{204}\text{Pb}$: 18.078–19.280, ϵ_{Nd} : +10.8 to +6.3) [Scheirer et al., 1996; Niu et al., 1996; Hall et al., 2006].

[6] Submersible and camera tow observations during the 1990s of fresh lava flows with little or no sediment cover and both diffuse and high-temperature hydrothermal venting [Renard et al., 1985; Auzende et al., 1994, 1996; Embley et al., 1998; Sinton et al., 2002] indicate that this region is one of frequent and recent volcanic activity [Auzende et al., 1996]. In January to February 1999, we conducted a field program designed to map and sample the products of individual eruptions on the SEPR between 17°25'S and 18°37'S. Nine *Alvin* dives were conducted between 17°25'S and 17°36'S [Sinton et al., 2002], supplementing observations and samples from *Nautile* and *Shinkai 6500* dives during 1993 and 1994, respectively [Auzende et al., 1996; Embley et al., 1998]. Lava samples were collected by wax core and dredge in areas not traversed during submersible operations.

2. Methods

2.1. Geological Observations

[7] Superposition of flow units, differences in sediment cover, and abrupt changes in flow morphology along dive track lines define lava flow boundaries and age relations among geologic units on the seafloor. We have integrated observations, dive transcripts, video and photographs from *Nautile* and *Alvin*, and geological interpretations from *Shinkai 6500* dives with DSL-120 side-scan sonar and bathymetry data [White et al., 2000] and chemical analyses of rock samples to create a geologic map showing the distribution of lava flow fields and geochemical lava types (Figure 1).

2.2. Microprobe Glass and Olivine Compositions

[8] Basalt glass separates from 156 samples were analyzed for major and minor elements by electron microprobe at the University of Hawai'i (UH) (Table 1). The reported chemical composition for each sample is an average of 5–12 analyses

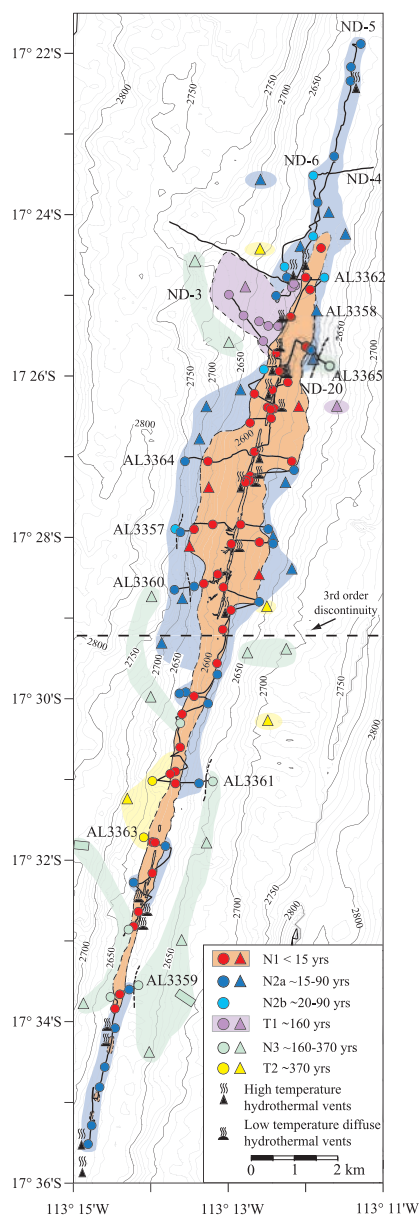


Figure 1. Geologic map of the southern EPR near 17°30'S, showing the distribution of lava groups discussed in the text. Boundaries of the N1 and T1 lava flow fields are based primarily on age differences observed during submersible operations (dashed where contacts are inferred). Colored areas without boundaries (N2, N3, and T2) highlight regions of similar lava type that are less well constrained by geologic observations. Posted ages are relative to 1993 A.D. and reflect the combined interpretation of geologic observations, and magnetic paleointensity and ($^{210}\text{Pb}/^{226}\text{Ra}$) disequilibria data. Lava less than several decades old (N1 and N2) surfaces the EPR at least 25 km along axis. Dive tracks from the NAUDUR (ND) and STOWA (AL) expeditions are shown as solid lines. Sample locations are shown as colored symbols, keyed to lava group for dive samples (circles), wax cores (triangles), and dredges (rectangles).

performed on three to four ultrasonically cleaned glass chips using an accelerating voltage of 15 kV, beam current of 10 nA, and 20 μm beam diameter, and normalized to oxide values for Makaopuhi glass standard A99. Samples were calibrated using glass standard A-99 (Si, Ti, Fe, Mg), Juan de Fuca glass standard VG-2 (Al, Ca, Na), and apatite (P) and orthoclase (K) mineral standards. Olivine phenocrysts in seven polished thin sections were analyzed with similar beam conditions using diopside (Si, Ca), olivine (Mg, Fe), garnet (Mn), and Ni metal (Ni) calibration standards. Complete sets of major and minor element glass data and olivine data are available as auxiliary material¹ files.

2.3. XRF Whole-Rock Compositions

[9] Fifty-three whole-rock samples were analyzed for major, minor and selected trace elements (Sc, V, Cr, Co, Ni, Cu, Zn, Rb, Sr, Y, Zr, and Nb) using a Siemens 303AS X-ray fluorescence (XRF) spectrometry system at UH (Tables 2a and 2b). Samples were broken with a tungsten-carbide-plated, hydraulic rock splitter, cleaned, and then crushed for approximately 5 minutes using an alumina mill. Two fused buttons for major elements and one pressed powder pellet for trace elements were prepared for each sample following procedures modified from those of *Norrish and Hutton* [1969] and *Chappell* [1991]. Each pressed powder pellet was analyzed twice for trace elements, averaged results are presented here. A complete set of whole-rock major and trace element data is available as an auxiliary material file.

2.4. Isotope and Isotope-Dilution Analyses

[10] Eleven basaltic glass samples were analyzed for Pb and Sr isotope composition and Pb concentrations by thermal ionization mass spectrometry (TIMS) using a VG Sector instrument at UH (Table 1); six of those samples were also analyzed for Nd isotopic composition. All isotopic composition and dilution measurements were made on fresh, generally phenocryst-free chips of hand-picked glass following procedures similar to those of *Mahoney et al.* [1992]. Selected U-series nuclides were analyzed at UH on ~ 1 g of fresh, hand-picked glass that was digested, dissolved and split into three aliquots for ^{226}Ra , ^{210}Pb and Th-U-Ba-Sr isotope dilution analysis, respectively. Th-U-Ba-Sr concentrations and (^{226}Ra) activities were

¹Auxiliary materials are available at <ftp://ftp.agu.org/apend/gc/2007gc001742>.

Table 1. Representative Major Element, Trace Element, and Isotopic Data for Glasses^a

Sample Unit	3360-8 N1	3361-7 N1	3363-7 N1	ND3-5 N1	ND19-8 N1	ND20-5 N1	3359-2 N2	3359-9B N2	ND6-1 N2	ND18-1 T1	3365-1 N3	3361-4 T2
Lat., S°	17.486	17.510	17.544	17.429	17.414	17.442	17.560	17.589	17.405	17.415	17.431	17.517
Long., W°	113.219	113.227	113.236	113.206	113.203	113.207	113.238	113.246	113.198	113.202	113.195	113.233
Depth, m	2572	2586	2592	2571	2578	2563	2598	2591	2590	2578	2622	2589
<i>n</i>	9	9	10	11	6	9	12	11	8	12	12	12
SiO ₂	50.3	50.0	50.4	50.1	50.1	50.5	50.3	49.5	50.1	49.8	50.2	49.7
TiO ₂	1.50	1.45	1.45	1.59	1.52	1.76	1.54	1.29	1.57	2.03	1.36	1.53
Al ₂ O ₃	14.8	15.0	15.1	14.6	14.6	14.4	14.4	15.8	14.9	14.2	15.1	16.2
FeO*	9.9	9.6	9.8	10.2	9.9	10.4	10.0	9.0	10.0	11.1	9.6	8.8
MnO	0.13	0.13	0.15	0.14	0.12	0.13	0.16	0.12	0.15	0.14	0.13	0.13
MgO	8.03	8.43	8.18	7.79	7.98	7.39	7.88	8.98	7.90	6.91	8.28	8.26
CaO	12.4	12.4	12.4	12.0	12.3	11.6	12.2	12.3	12.1	11.4	12.6	11.8
Na ₂ O	2.48	2.47	2.47	2.49	2.51	2.73	2.52	2.33	2.53	2.95	2.48	2.80
K ₂ O	0.10	0.10	0.10	0.11	0.11	0.12	0.10	0.10	0.13	0.22	0.08	0.15
P ₂ O ₅	0.11	0.11	0.12	0.12	0.11	0.13	0.11	0.09	0.13	0.17	0.09	0.15
Total	99.7	99.8	100.1	99.1	99.4	99.3	99.3	99.6	99.5	99.0	99.9	99.6
Rb	0.9	0.8	0.8	0.9	1.0	0.8	0.8	0.8	1.3	2.2	0.4	1.1
Sr	120.2	121.4	119.7	118.9	118.3	110.8	110.1	127.9	118.2	140.2	115.0	161.0
Y	34.4	31.7	32.2	37.9	35.0	40.1	34.4	28.3	33.3	44.5	30.6	33.0
Zr	93.4	87.5	88.7	101.4	96.2	106.3	91.5	82.0	98.9	161.1	81.5	121.6
Nb	2.9	2.7	2.6	2.9	3.0	2.6	2.5	2.6	3.5	5.7	1.6	3.7
Ba (TIMS)	9.31	8.66	8.79	8.45	9.49	7.02	8.04	8.72	12.95	21.64	4.03	8.16
La	3.0	2.9	2.9	3.1	3.1	3.1	2.9	2.7	3.5	5.0	2.3	4.2
Ce	9.4	9.0	8.9	9.7	9.4	9.9	9.0	8.4	10.4	14.7	7.5	12.8
Pr	1.6	1.6	1.5	1.7	1.6	1.8	1.6	1.4	1.7	2.4	1.4	2.1
Nd	8.5	8.1	8.1	8.9	8.5	9.3	8.3	7.4	9.0	11.9	7.3	10.2
Sm	2.9	2.8	2.8	3.1	3.0	3.3	3.0	2.5	3.0	3.9	2.7	3.2
Eu	1.0	1.0	1.0	1.1	1.1	1.1	1.0	0.9	1.1	1.3	1.0	1.1
Gd	3.6	3.4	3.5	3.9	3.6	4.1	3.7	3.0	3.7	4.7	3.3	3.8
Tb	0.71	0.67	0.67	0.76	0.71	0.81	0.72	0.59	0.72	0.90	0.64	0.71
Dy	4.8	4.5	4.5	5.1	4.8	5.4	4.8	3.9	4.8	6.0	4.3	4.6
Ho	1.1	1.0	1.0	1.1	1.1	1.2	1.1	0.9	1.1	1.3	1.0	1.0
Er	2.9	2.7	2.7	3.1	2.9	3.3	2.9	2.4	2.9	3.6	2.6	2.8
Tm	0.44	0.41	0.41	0.47	0.44	0.51	0.45	0.36	0.44	0.55	0.40	0.42
Yb	2.8	2.7	2.7	3.0	2.8	3.3	2.9	2.3	2.8	3.5	2.6	2.7
Lu	0.44	0.42	0.42	0.47	0.44	0.51	0.45	0.36	0.44	0.56	0.40	0.42
Hf	2.3	2.2	2.2	2.5	2.3	2.6	2.3	2.0	2.4	3.2	2.0	2.6
Ta	0.23	0.20	0.21	0.20	0.20	0.20	0.19	0.17	0.25	0.37	0.22	0.25
Pb (TIMS)	0.362	0.353	0.383	0.312	0.359	0.367	0.351	0.311	0.379	0.499	0.253	0.499
Th (TIMS)	0.1717	0.1708	0.1579	0.1594	0.1748	0.1477	0.1525	0.1586	0.2258	0.3398	0.0822	0.2202
U (TIMS)	0.0628	0.0601	0.0582	0.0611	0.0661	0.0602	0.0574	0.0578	0.0850	0.1226	0.0349	0.0831
⁸⁶ Sr/ ⁸⁷ Sr	0.70271	0.70271	0.70272	0.70269	0.70270	0.70268	0.70269	0.70271	0.70271	0.70270	0.70266	0.70256
¹⁴³ Nd/ ¹⁴⁴ Nd	-	0.513075	-	-	-	0.513099	-	0.513056	0.513089	0.513094	-	0.513119
ϵ_{Nd}	-	+8.5	-	-	-	+9.0	-	+8.1	+8.8	+8.9	-	+9.3
²⁰⁶ Pb/ ²⁰⁴ Pb	18.755	18.799	18.770	18.725	18.756	18.681	18.721	18.864	18.798	18.761	18.615	18.548
²⁰⁷ Pb/ ²⁰⁴ Pb	15.529	15.541	15.520	15.517	15.540	15.512	15.531	15.548	15.536	15.515	15.505	15.499
²⁰⁸ Pb/ ²⁰⁴ Pb	38.320	38.376	38.301	38.260	38.357	38.220	38.304	38.440	38.369	38.320	38.126	38.083

^a Major and minor elements were measured by electron microprobe (Cameca SX-50) at the University of Hawai'i. FeO*, total Fe as FeO; *n*, number of microprobe analyses in each sample group averaged for major element composition. Mean 2σ precision (in parentheses) for sample groups: SiO₂ (0.41), TiO₂ (0.08), Al₂O₃ (0.17), FeO* (0.26), MnO (0.05), MgO (0.13), CaO (0.18), Na₂O (0.13), K₂O (0.02), and P₂O₅ (0.03). A complete set of major and minor element glass data is available as auxiliary material Table S1. Trace elements were measured by ICP-MS (Element 2) except where noted; values are means of three individual analyses performed at the University of Hawai'i. Mean trace element concentrations and standard deviations (in ppm) of 9 repeat analyses of rock standard BHVO-1 are Rb (9.3, 0.2), Sr (402, 3.4), Y (30.2, 1.1), Zr (178, 2.6), Nb (19.3, 0.6), La (15.8, 0.27), Ce (39.2, 0.7), Pr (5.7, 0.12), Nd (25.1, 0.9), Sm (5.95, 0.1), Eu (1.97, 0.03), Gd (6.15, 0.18), Tb (0.93, 0.01), Dy (5.17, 0.09), Ho (0.98, 0.01), Er (2.39, 0.04), Tm (0.31, 0.02), Yb (2.01, 0.04), Lu (0.29, 0.005), Hf (4.4, 0.12), and Ta (1.22, 0.04). Ba, Pb, Th, and U concentrations were determined by TIMS on VG Sector and Sector 54-WARP instruments at the University of Hawai'i; precision is 0.3% for Ba, Th, and U and 1% for Pb. Isotope ratios are reported relative to the measured value of ⁸⁷Sr/⁸⁶Sr = 0.710238 for NBS 987 Sr, to ¹⁴³Nd/¹⁴⁴Nd = 0.511845 for La Jolla Nd, and the Pb isotope values of *Todt et al.* [1996] for NBS 981 Pb. Uncertainties (2σ) for individual analyses are less than or equal to the external uncertainties for these standards (NBS 987 Sr ±0.000016, La Jolla Nd ±0.000008 or ±0.2 ε_{Nd} units, NBS 981 Pb ±0.011 for ²⁰⁶Pb/²⁰⁴Pb and ²⁰⁷Pb/²⁰⁴Pb, ±0.031 for ²⁰⁸Pb/²⁰⁴Pb). ε_{Nd} = 0 corresponds to ¹⁴³Nd/¹⁴⁴Nd = 0.51264. Total procedural blanks are 12–35 pg for Pb, <35 pg for Sr, and <10 pg for Nd.

Table 2a. Whole-Rock Major, Minor, and Trace Element Analyses by X-Ray Fluorescence^a

Sample Unit	3360-8 N1	3361-7 N1	3363-7 N1	ND3-5 N1	ND19-8 N1	ND20-5 N1	3359-2 N2	3359-9B N2	ND6-1 N2	ND18-1 T1	3365-1 N3	3361-4 T2
Lat., °S	17.486	17.510	17.544	17.429	17.414	17.442	17.560	17.589	17.405	17.415	17.431	17.517
Long., °W	113.219	113.227	113.236	113.206	113.203	113.208	113.238	113.246	113.198	113.202	113.195	113.233
Depth, m	2572	2586	2592	2571	2578	2563	2598	2591	2590	2578	2622	2589
SiO ₂	50.68	50.23	49.98	50.68	50.93	51.00	51.21	49.51	50.44	50.77	49.58	49.67
TiO ₂	1.54	1.45	1.45	1.63	1.54	1.74	1.56	1.32	1.59	2.02	1.34	1.57
Al ₂ O ₃	15.03	15.18	15.16	14.97	14.97	14.56	14.54	16.08	15.21	14.50	15.42	16.43
FeO*	10.24	9.78	9.84	10.42	10.25	10.80	10.54	9.22	10.19	11.44	9.61	8.92
MnO	0.18	0.19	0.17	0.18	0.18	0.19	0.16	0.16	0.18	0.20	0.17	0.18
MgO	8.03	8.40	8.27	7.76	7.88	7.34	8.03	8.90	7.86	6.86	8.23	8.41
CaO	12.39	12.23	12.19	12.05	12.30	11.68	12.26	12.29	12.11	11.47	12.54	11.69
Na ₂ O	2.48	2.47	2.58	2.49	2.51	2.73	2.52	2.29	2.53	2.95	2.48	2.80
K ₂ O	0.09	0.09	0.11	0.08	0.08	0.09	0.08	0.09	0.11	0.20	0.06	0.19
P ₂ O ₅	0.12	0.09	0.12	0.13	0.11	0.15	0.13	0.11	0.14	0.19	0.10	0.14
Total	100.34	99.90	99.89	100.27	100.24	99.97	100.65	99.98	99.85	100.15	99.12	99.80
LOI ^a	-0.51	-0.77	-0.66	-0.59	-0.59	-0.70	-0.56	-0.37	-0.46	-0.43	-0.46	-0.16
Sc	47	44	47	51	51	48	47	44	49	51	48	39
V	352	325	328	368	353	386	369	282	355	404	292	274
Cr	367	367	371	325	363	233	339	393	316	180	401	338
Co	46	41	43	45	44	42	45	47	44	42	46	41
Ni	99	114	111	92	90	77	90	145	99	55	102	140
Cu	-	83	84	81	85	78	-	-	82	80	-	74
Zn	84	80	86	85	84	90	84	74	82	95	75	74
Rb	1.6	1.1	1.3	1.3	1.5	1.1	1.8	1.5	1.8	3.0	1.3	1.4
Sr	113	115	113	109	111	104	107	125	117	133	111	158
Y	33	30	30	34	32	38	34	28	32	41	29	30
Zr	93	88	88	98	93	107	92	82	98	137	81	119
Nb	2.9	2.7	3.2	3.3	3.2	2.8	2.3	3.1	4.0	5.8	1.9	3.7

^a All analyses by XRF (Siemens 303-AS) at the University of Hawaii. FeO*, total Fe as FeO. LOI is weight total loss on ignition at 900° for 8 hours. A complete set of 52 XRF analyses is available as auxiliary material Table S2.

determined by isotope dilution TIMS on the Sector 54-WARP using calibrated ²²⁹Th, ²³³U, ¹³⁵Ba, ⁸⁴Sr and ²²⁸Ra tracers. (²¹⁰Pb) activities were determined by high-resolution alpha spectrometry using a calibrated ²⁰⁹Po tracer. Analytical methods are detailed by Rubin *et al.* [2005], who first reported (²¹⁰Pb/²²⁶Ra) results for NAUDUR (ND) samples. We denote activities and activity ratios with parentheses.

2.5. ICP-MS Trace Element Data

[11] Trace element data for selected samples were obtained on fresh, hand-picked glass chips by inductively coupled plasma mass spectrometry, using an Element 2 instrument and rock standard calibration at UH. Data are means of three consecutive analyses of the same solution (Table 1).

2.6. Age Constraints

[12] Understanding absolute timescales is essential in any geologic study, but accurate dating of youthful submarine lava has proven to be a difficult task. This study employed three methods: field observations, (²¹⁰Pb/²²⁶Ra) geochronology and magnetic paleointensity, to constrain relative

and absolute eruption ages and magmatic process timescales.

2.6.1. Geologic Constraints

[13] The two primary field observations used to constrain relative ages of lava units were superposition (stratigraphic relationships) and sediment cover. Sediment cover provides a crude but effective method for estimating relative ages of lava in an environment of steady deposition and limited reworking. The method can be complicated by local hydrothermal venting, bottom currents, and how sediments coat different lava morphologies (low-relief surfaces are more easily covered at uniform sediment thickness). Nevertheless we were able to document flow contacts with differences in sediment cover from the submersible, providing a relative eruption chronology.

2.6.2. (²¹⁰Pb/²²⁶Ra) Radioactive Disequilibria

[14] (²¹⁰Pb/²²⁶Ra) radioactive disequilibria have been used often to constrain the timescales of

Table 2b. BHVO-1 Whole-Rock Major, Minor, and Trace Element Analyses by X-Ray Fluorescence^a

	BHVO-1		Ref. Val
	Mean	Std. Dev	
SiO ₂	49.69	0.16	49.59
TiO ₂	2.74	0.04	2.69
Al ₂ O ₃	13.69	0.06	13.70
Fe ₂ O ₃	12.38	0.03	12.39
MnO	0.16	0.01	0.17
MgO	7.28	0.05	7.22
CaO	11.33	0.04	11.32
Na ₂ O	2.37	0.20	2.24
K ₂ O	0.51	0.01	0.52
P ₂ O ₅	0.29	0.01	0.27
Total	100.44		100.11
Sc	30.2	1.5	31.8
V	308	6.7	317
Cr	305	3.3	289
Co	43.5	1.6	45
Ni	123	4.4	121
Zn	105	4.0	105
Rb	9.8	0.4	9.5
Sr	394	3.8	390
Y	26.4	0.4	27.6
Zr	174	3.0	179
Nb	18.6	0.5	19

^a An indication of accuracy is provided by measured and recommended (ref.) values (n = 10) for standard BHVO-1, which was run as an unknown during the analyses.

crustal magmatic processes, until recently primarily in island arc or oceanic island settings [Oversby and Gast, 1968; Rubin and Macdougall, 1989; Rubin *et al.*, 1989; Gill and Williams, 1990; Sigmarsson, 1996; Gauthier and Condomines, 1999; Turner *et al.*, 2004]. With a half-life of ~22 a, disequilibria between these two U-series nuclides has potential for elucidating magmatic processes occurring ~10–120 a ago. Rubin *et al.* [2005] studied (²¹⁰Pb/²²⁶Ra) disequilibria in historic mid-ocean ridge basalt (MORB) from the Juan de Fuca Ridge (JdFR), the northern EPR, and this area of the SEPR and found that the degree of disequilibria (as ²¹⁰Pb deficits) was strongly anti-correlated with geochemical indicators of low pressure magmatic differentiation. On this basis and because (²¹⁰Pb/²²⁶Ra) was well correlated with (²²⁶Ra/²³⁰Th) they proposed that Pb-Ra fractionation in MORB resulted from mantle melting. This requires not only that lava with measurable (²¹⁰Pb/²²⁶Ra) disequilibria has been on the seafloor for significantly less than ~120 a, but also that combined melting, transport, and residence times in shallow magma reservoirs is very short, amounting in total to a few decades.

2.6.3. Magnetic Paleointensity

[15] The magnetic paleointensity of submarine basaltic glass can be used as a chronometer by comparison to known geomagnetic field intensity variations [Pick and Tauxe, 1993; Kent and Gee, 1996; Mejia *et al.*, 1996; Carlut and Kent, 2000; Carlut *et al.*, 2004]. Seven samples from this area were analyzed as part of a study of the effect of cooling rate on paleointensity in submarine basaltic glass [Bowles *et al.*, 2005], providing age estimates for geologic units that are further interpreted here. Details of the Thellier-type magnetic paleointensity methods at Scripps Institution of Oceanography are given by Bowles *et al.* [2005]. Eruption age estimates were calculated by comparing magnetic intensity values for each sample with models of geomagnetic field intensity variations derived from historical measurements [Jackson *et al.*, 2000].

[16] Unfortunately, there is little knowledge of the absolute magnitude or rate of change in geomagnetic field intensity prior to ~1840 A.D. Additionally, Bowles *et al.* [2006] found that some MORB of known age near 9°50'N EPR yielded paleointensities lower than expected, resulting in model ages less than actual ages. The cause of this bias or whether it may be expected to occur in other geographic regions is unclear. Although paleointensity ages presented here are generally consistent with age constraints from other methods, observations and model limitations suggest that the true uncertainty of calculated ages, especially for older samples, may be significantly larger than analytical error implies.

3. Results

3.1. Geologic Units

[17] The distribution of lava flow fields and geochemical lava types is shown in Figure 1. Samples of the mapped terrain are divided into five groups on the basis of systematic geological (Figure 2) and/or geochemical differences (Figure 3) and have been assigned N or T prefixes on the basis of normal MORB or transitional MORB-like compositional affinities (T-MORB here being defined as those lavas with K/Ti > 0.12 and K₂O > 0.15). The distribution of N1 and T1 units were mapped primarily with field observations. The remaining sample sites fall outside the boundaries of the two geologically well-defined units and are divided into N2, N3, and T2 groups by variations in chemical composition and by limited geological observation. Other samples collected by wax core or dredge

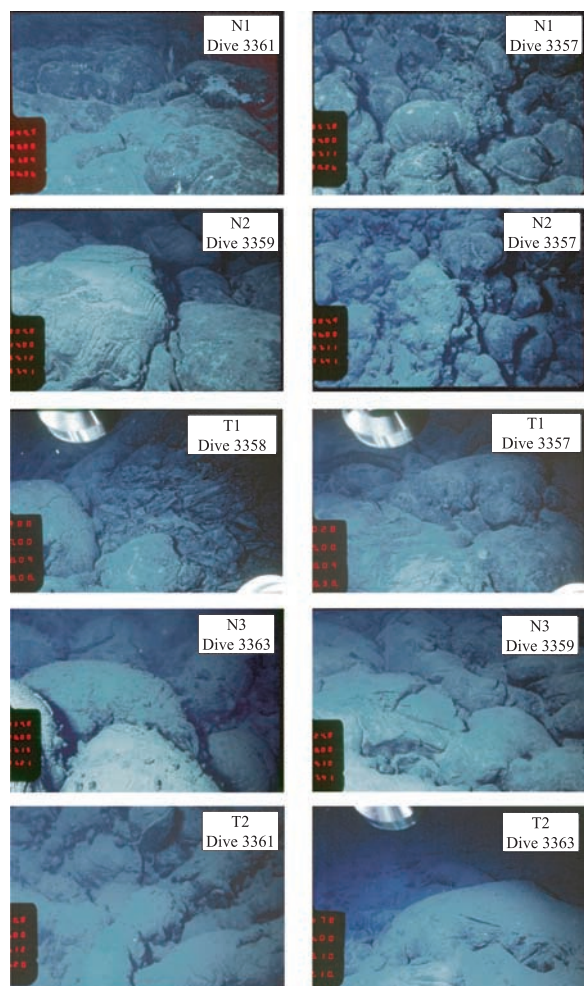


Figure 2. Photographs of the seafloor showing differences in sediment cover on lava from the five major geologic units/magma types described in the text, which increase in age from top to bottom. Note significant differences in sediment cover between the youngest and oldest units; differences between the youngest units (N1 and N2), perhaps erupted only years to decades apart, are more subtle.

lack geologic context yet their locations are well known. We cannot preclude an off-axis origin for some wax core or dredge samples but the lack of observed off-axis vent structures and proximity of all lava types to the topographic axis (<200 m) leads us to believe that all geologic units recognized are products of on-axis eruptions.

3.1.1. N1 Lava (N-MORB 1)

[18] The youngest and best-mapped geologic unit is the N1 flow field (also referred to as the Aldo-Kihi flow field [Auzende *et al.*, 1996; Sinton *et al.*, 2002] or L0 flow [Embley *et al.*, 1998]) that straddles the ridge axis between 17°24'S and

17°34'S; at least three discontinuous patches of young lava outcrop farther south along the axis to ~17°35'S (Figure 1). The N1 flow field extends ~19 km along the axis with an area of 14 km² and a maximum width of 2.2 km (at 17°27'S). At this widest spot the flow field is dominantly lobate lava interspersed with moderately high effusion/flow rate lavas (channels floored by lineated and jumbled sheet flows trending along and across the axis). Between 17°26' and 17°28'S, there are seven 100- to 500-m-long en echelon summit collapse troughs, each ≤50 m wide. Just to the north (17°28' to 17°28.5'S) a 220-m-long and 30-m-wide branching, partially collapsed lava distribution system (first noted on 120 KHz side-scan sonar images) trends down the west side of the axis. Estimated thicknesses of lobate lava from collapse pits on the ridge axis exceed 12 m locally. Collapse features are much less prevalent between 17°29' and 17°34'S, where the flow field is much narrower (150–500 m across axis) and estimated volume of extruded lava is much less. Lower effusion rate pillow and lobate lava morphologies are dominant south of 17°29'S. Subtle variations in sediment cover and geological relations such as lava cascading into collapse pits indicate that the N1 flow field had more than one eruptive phase [Sinton *et al.*, 2002]. As a group, however, N1 lava can be readily distinguished from older units (Figure 2), and we consider the entire field to represent the products of a prolonged eruptive episode comprising a series of discrete eruptive events [Sinton *et al.*, 2002] that must have occurred just prior to submersible operations in 1993 (see below).

[19] MgO contents of 67 N1 glasses range from 7.3–8.4 wt%; TiO₂, FeO*, Na₂O, K₂O, and P₂O₅ contents increase with decreasing MgO (Figure 3). Al₂O₃ decreases with decreasing MgO and there is an inflection in CaO/Al₂O₃ at ~7.9 wt% MgO. K/Ti values within the N1 flow range from 0.09 to 0.12. Although the major element data show coherent trends that vary with MgO, the range of radiogenic isotope and trace element data requires a compositionally heterogeneous mantle source (i.e., the N1 lava cannot be derived by differentiation from a single or small range of primary magmas; Figure 4). ²⁰⁶Pb/²⁰⁴Pb ratios range from 18.681 to 18.799; although ⁸⁷Sr/⁸⁶Sr (0.70268 to 0.70271) and ε_{Nd} (+9.0 to +8.5) vary little outside of analytical error. Th/U, Zr/Y, and Sr concentrations are positively correlated with MgO content (Figure 5), inconsistent with fractional crystallization.

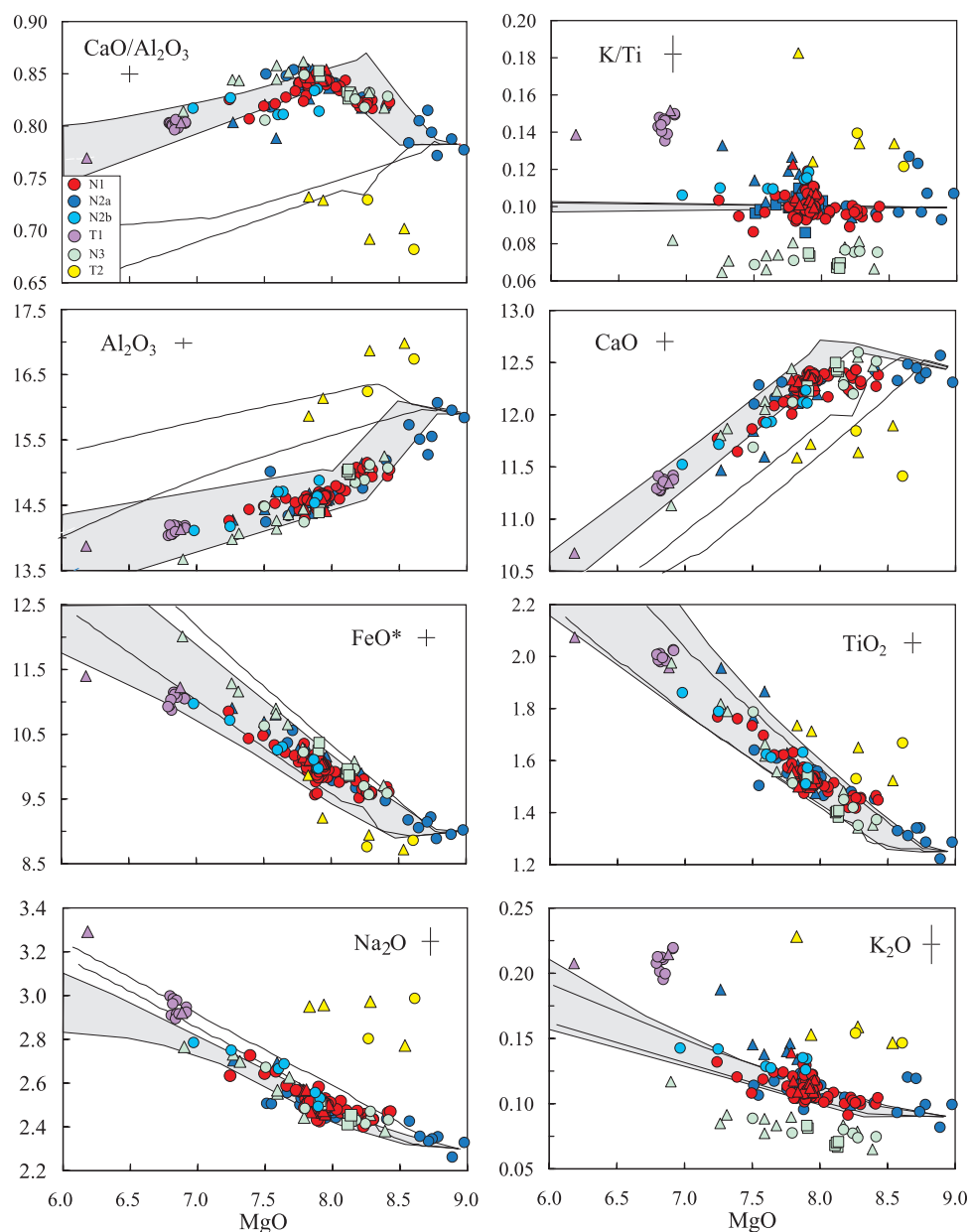


Figure 3. Major and minor element variation of glass samples from the 17°30'S area; data obtained by electron microprobe. Symbols are the same as in Figure 1. The decrease in Al_2O_3 with decreasing MgO indicates fractionation of both plagioclase and olivine. The change in slope in $\text{CaO}/\text{Al}_2\text{O}_3$ at 7.9 wt% MgO reflects the onset of Ca-rich clinopyroxene fractionation. Note the distinctly lower K_2O and slightly higher average FeO^* contents of N3 samples relative to the other sample groups at the same MgO. T-MORB groups T1 and T2 are enriched in K_2O relative to the other N-MORB groups. Gray field encompasses MELTS equilibrium and fractional crystallization trends for 0.5 kbar with 0.1–0.3 wt.% H_2O using an oxygen fugacity of QFM-2. Light and heavy black lines are MELTS fractional crystallization paths run at 2 kbar with 0.1 and 0.3 wt.% H_2O , respectively. Overall major element trends are consistent with crystallization processes taking place in the upper 1–2 km of the oceanic crust.

3.1.2. N2 (N-MORB 2)

[20] N2 covers a larger geographical area than N1, extending ~25 km along-axis and ~2.8 km across-axis at 17°28.5'S (Figure 1). The full extent of N2 lava is undefined because it extends at least to the

northern and southern extremes of dive coverage at 17°23'S and 17°35.8'S and also to the cross-axis limits of some dives. Lobate and pillow lava are common, with rare patches of jumbled sheet flow within lava channels. Axis-parallel fissures up to more than a meter wide cleanly truncate lobes and

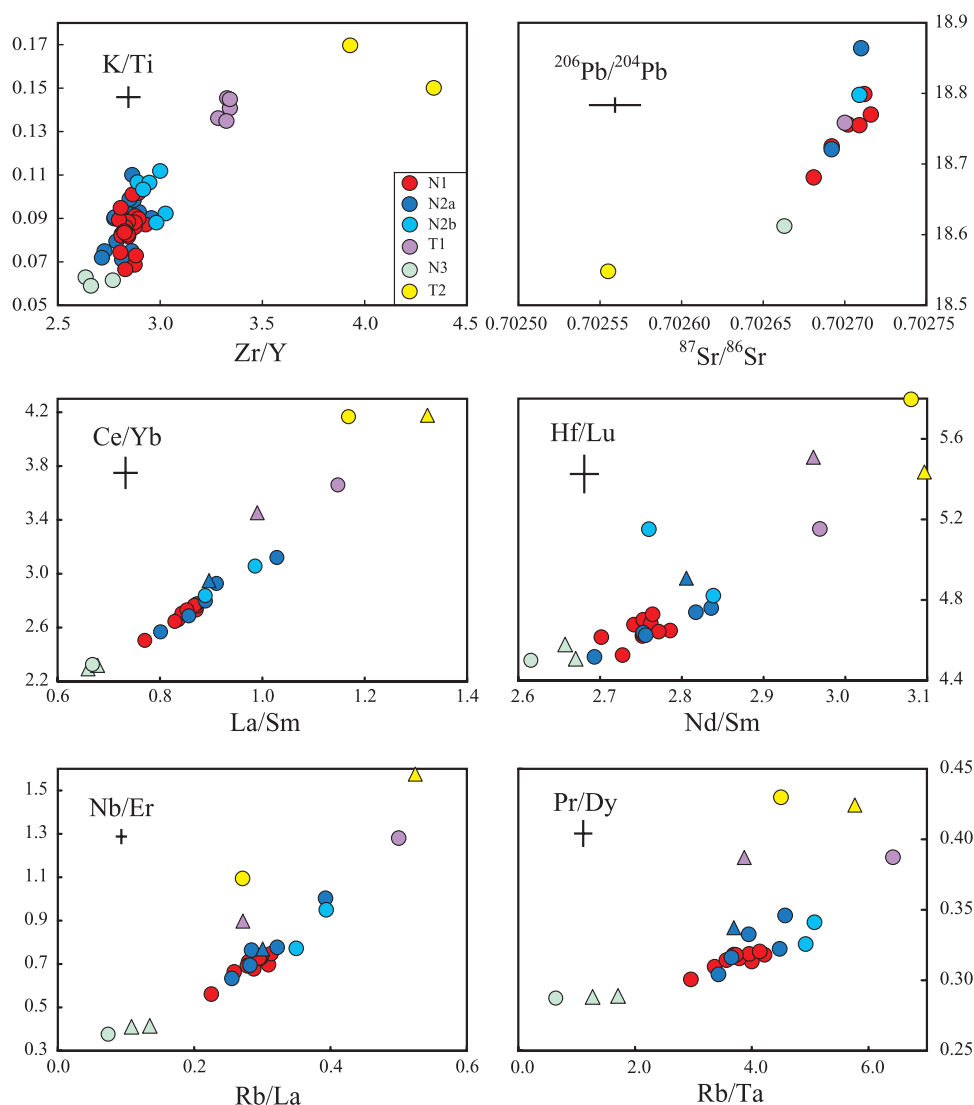


Figure 4. Pb and Sr isotope and trace element ratio variation diagrams illustrate compositional ranges within and differences among the five magma groups described in the text. N1 and N2, which are distinguished by geological observations, show broad, overlapping compositional ranges. N-MORB samples form a trend that is consistent with mantle source variation; T-MORB samples have generally elevated ratios of highly incompatible to moderately incompatible elements, suggesting derivation from smaller degrees of partial melting than for N-MORB. K, Ti, Zr, and Y data by XRF on whole-rock samples; Pb and Sr isotope data on volcanic glass by TIMS; other trace element on glass by ICP-MS.

pillows on the uppermost surface of the N2 flow and so post-date it. Both high- and low-temperature hydrothermal venting emanated from N2 lava near the axis in 1993, 1994, and 1996 [Auzende *et al.*, 1996; Embley *et al.*, 1998; Hobson *et al.*, 1997].

[21] N2 major element trends are broadly similar to N1 but span a greater range of MgO (7.0–9.0 wt%, Figure 3). Like N1, N2 lava has isotope and trace element variability that cannot be explained by simple differentiation from a single parental magma (Figures 4 and 5). $^{206}\text{Pb}/^{204}\text{Pb}$ ratios (18.721 to

18.864), including the most radiogenic sample within the study area, and ϵ_{Nd} (+8.8 to +8.1) varies substantially (Figure 5 and Table 1); $^{87}\text{Sr}/^{86}\text{Sr}$ ratios are nearly uniform at about 0.70270. Th/U, Zr/Y, and Sr concentrations are positively correlated with MgO content, similar to those for N1 (Figure 5).

[22] Geological observations, age constraints, and geochemical characteristics suggest that N2 comprise a single geological unit, yet within it we recognize two subgroups, hereafter referred to as

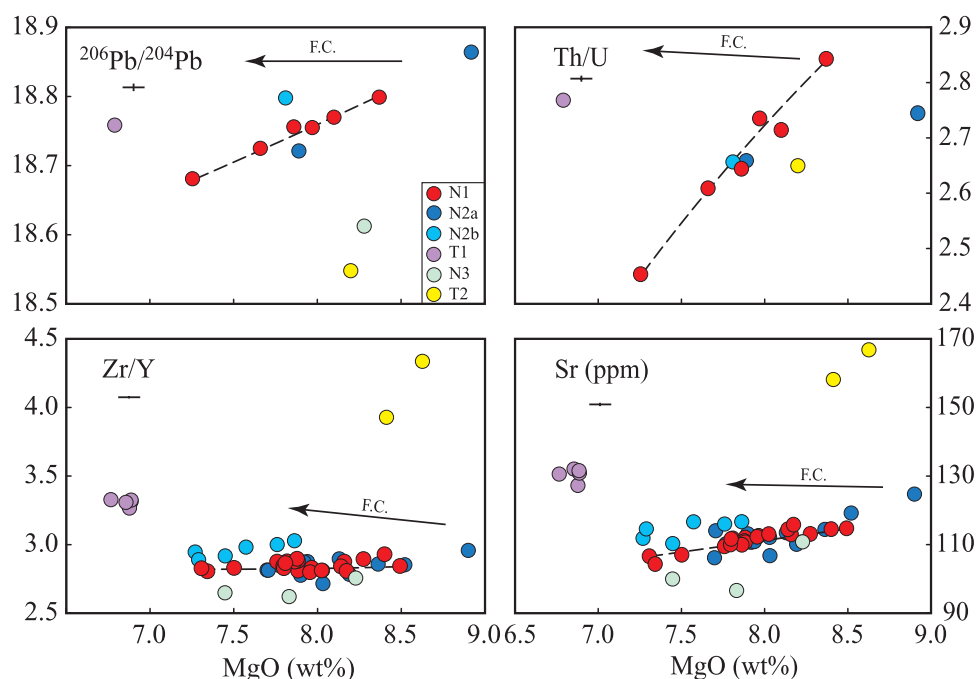


Figure 5. Variations in isotopic and chemical variations versus MgO are inconsistent with shallow-level fractional crystallization of a single parental magma composition. Differentiation trajectories (labeled F.C.) were calculated from phase proportions derived by MELTS [Ghiorsio and Sack, 1995] and published distribution coefficients [Villemant et al., 1981; McKenzie and O'Nions, 1991; Beattie et al., 1993; Hart and Dunn, 1993; Nikogosian and Sobolev, 1997; Bindeman et al., 1998]. Dashed lines show two-component mixing curves between high- and low-MgO end-members of N1 lava. For N-MORB groups, the variation suggests mixing between high-temperature, incompatible element-enriched and lower-temperature, incompatible element-depleted magmas derived from a less radiogenic source. Pb isotope and Th/U data by TIMS on volcanic glass; Zr/Y and Sr data by XRF on whole-rock samples.

N2a and N2b, based on subtle compositional distinctions and location. The six N2b samples occur in a restricted area between 17°23.5'S and 17°28'S, and are more differentiated than N2a. Zr/Y ratios, and Sr, Th, and U concentrations for N2b lavas are all elevated at a given MgO content relative to N2a lava, generally trending toward T1 compositions (Figures 4 and 5). The N2 flow field may thus represent the combined products of an eruptive episode composed of individual, shorter-lived eruptive events.

3.1.3. T1 (T-MORB 1)

[23] The T1 flow field (called the Rehu-Marka flow by Sinton et al. [2002] after hydrothermal vent sites on it [Fouquet et al., 1994; Urabe et al., 1995], is located on the western flank of the EPR axis between 17°24'S and 17°26'S (Figure 1). It extends ~2 km from the axis [Sinton et al., 2002]. Dive observations show that the distal part of the flow is dominated by jumbled sheet lava overlain by lobate lava closer to the axis, consistent with

effusion rates that waned as the eruption progressed.

[24] T1 is the most differentiated geologic unit in the area and chemical compositions of 12 glass samples from the flow are extremely uniform over its mapped extent. Measurements for most of the major and minor elements are identical within error (Figure 3); trace element concentrations for five samples analyzed by XRF are similarly homogeneous. Although the homogeneity of this unit is distinctive for the area, it also is geographically restricted and not substantially more homogeneous than other lava groups over an equivalent areal extent. An additional more differentiated wax core sample with similar K/Ti and Zr/Y is included in this group. Sr, Nd, and Pb isotope data for one T1 sample are similar to median values for the area (Table 1); thus elevated K₂O, Sr, Th, and U concentrations and Zr/Y and Nd/Sm ratios relative to other magma groups cannot be accounted for by an enriched source or by greater extents of differentiation. This requires that T1 lava is derived from

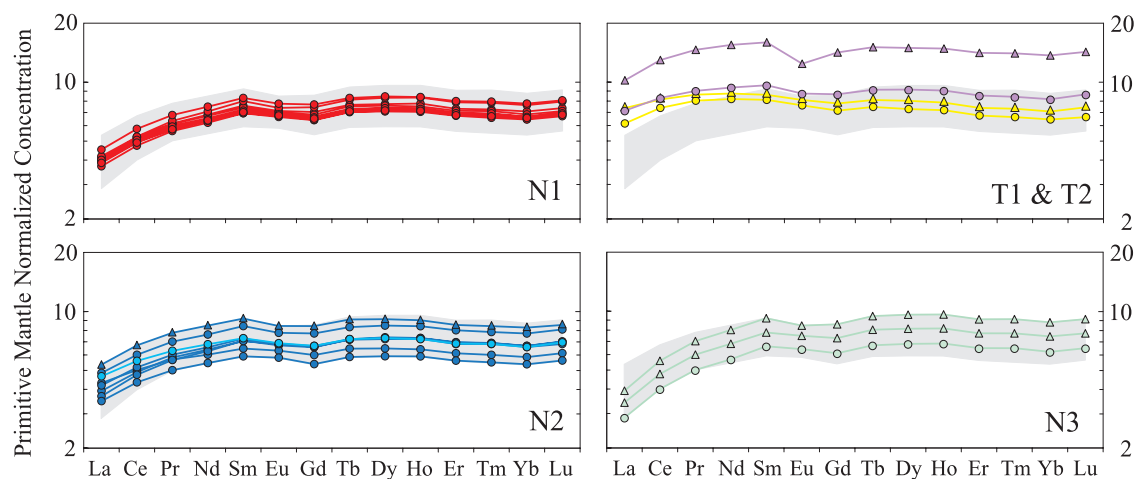


Figure 6. Primitive mantle-normalized rare earth element (REE) patterns separated by magmatic unit. Gray area represents range of N-MORB concentrations within this study area. N1 and N2 lava are moderately depleted in light REEs and overlap with each other. N3 lava shows greater light REE depletion than younger N-MORB groups. T1 and T2 show less light REE depletion than N-MORB groups. All data by ICP-MS on glass separates.

a relatively incompatible element-enriched parental magma (Figures 3 and 5 and Table 1).

3.1.4. N3 (N-MORB 3)

[25] N3 is distinguishable from N1 and N2 lava by observations of significantly greater sediment cover and different lava morphology on *Alvin* dives 3359, 3361 and 3365 (Figure 2). No ($^{210}\text{Pb}/^{226}\text{Ra}$) disequilibria or magnetic paleointensity data exist for N3 lava but it clearly predates N2 (Figure 1). N3 samples collected by submersible have K_2O values ~ 0.03 wt% lower than N1 and N2 at similar MgO contents (Figure 3). Sixteen additional samples collected by wax core and dredge were included on the basis of similar geochemistry and sample geography. N3 samples were recovered from both flanks of the EPR between 100 m and 2.7 km from the axis at $17^\circ 24.3'$ to $17^\circ 34.2'\text{S}$ (Figure 1). The majority of samples occur south of $17^\circ 28.7'\text{S}$, possibly because the middle and northern parts of the study area have been extensively resurfaced by younger flows. The N3 flow is dominated by pillow and lobate lavas, although one sample (AL3361-1) is from a jumbled sheet flow.

[26] Incompatible trace element concentrations and ratios of highly incompatible to moderately incompatible elements for N3 lava are generally lower than those of other units at the same MgO content (Figures 4, 5, and 6). Sample 3365-1 has relatively unradiogenic $^{206}\text{Pb}/^{204}\text{Pb}$ (18.615) and $^{87}\text{Sr}/^{86}\text{Sr}$ (0.70266) values, consistent with trace element data suggesting derivation from a more incompat-

ible element-depleted mantle source than the other N-MORB groups. N3 samples have lower K_2O , slightly lower mean P_2O_5 , and slightly higher mean FeO^* contents than the other lava units at given MgO (Figure 3). MgO contents (6.9 to 8.4 wt%) and other major element compositions in N3 are similar to N1 and N2 lava.

3.1.5. T2 (T-MORB 2)

[27] T2 lava was identified as heavily sedimented terrain just outside the western boundary of the N1 lava near $17^\circ 31'\text{S}$; only two T2 samples were collected by submersible; the flow near $17^\circ 31.5'\text{S}$ includes pillow, lobate, and sheet forms. Four additional wax core samples are included in the group on the basis of similar chemical composition (Figure 3). Five of the six samples are clustered between $17^\circ 28.8'\text{S}$ and $17^\circ 31.8'\text{S}$, the remaining sample is located just north of the T1 flow field (Figure 1).

[28] T2 lava is the most compositionally distinct magma type in the study area with relatively elevated TiO_2 , Al_2O_3 , and Na_2O , and low FeO^* and CaO levels (Figure 3). Incompatible trace element concentrations and highly incompatible to moderately incompatible trace element ratios are substantially higher than other lava units at the same MgO (Figures 4, 5, and 6), whereas $^{206}\text{Pb}/^{204}\text{Pb}$, $^{87}\text{Sr}/^{86}\text{Sr}$, and ϵ_{Nd} values for one T2 sample (18.548, 0.70256, and +9.3, respectively) are the least radiogenic values of this study (Figure 4).

Table 3. Magnetic Paleointensity and Pb/Ra Disequilibria Age Constraint Data^a

Sample Unit	3360-8 N1	3361-7 N1	3363-7 N1	ND3-5 N1	ND19-8 N1	ND20-5 N1	3359-2 N2	3359-9B N2	ND6-1 N2	ND18-1 T1	3361-4 T2
Site mean, μT	32.2	-	28.6	30.0	-	-	32.5	-	33.9	38.0	45.1
Error (1 σ)	0.7	-	2.2	0.8	-	-	0.5	-	1.0	0.7	1.7
Age, a	19	-	-60	-30	-	-	26	-	55	156	370
Upper limit, a	-16	-	?	-62	-	-	2	-	17	116	319
Lower limit, a	51	-	36	5	-	-	47	-	100	195	?
$(^{210}\text{Pb})/(^{226}\text{Ra})_{\text{m}}$	0.955	0.971	0.949	0.950	0.930	0.964	0.948	0.973	0.936	1.005	0.998
\pm	0.030	0.024	0.018	0.020	0.017	0.024	0.018	0.022	0.015	0.015	0.020
$(^{210}\text{Pb})/(^{226}\text{Ra})_{\text{i}}$	0.941	0.961	0.933	0.944	0.920	0.957	0.931	0.963	0.923	1.005	0.997
\pm	0.032	0.026	0.020	0.021	0.018	0.025	0.020	0.024	0.017	0.017	0.022

^a All magnetic paleointensity data are from *Bowles et al.* [2005]; Pb/Ra disequilibria data for NAUDUR (ND) samples are from *Rubin et al.* [2005]. Upper and lower age limits for paleointensity data are based on experimentally derived 2σ uncertainties combined with the paleomagnetic field model of *Jackson et al.* [2000] evaluated for this study site. Actual age uncertainties, especially for older samples, may be greater than those listed because of uncertainties in the paleomagnetic field model. Negative paleomagnetic ages reflect measured intensities less than the 1993 model value of 31.3 μT . ^{226}Ra nuclides were determined by high abundance sensitivity thermal ionization mass spectrometry, ^{210}Pb by α -counting. Parentheses denote activity ratios calculated from atomic abundance analyses using $\lambda^{226}\text{Ra} = 4.332 \times 10^{-4} \text{ a}^{-1}$ and $\lambda^{210}\text{Pb} = 3.108 \times 10^{-2} \text{ a}^{-1}$. $(^{210}\text{Pb})/(^{226}\text{Ra})_{\text{m}}$ are activity ratios measured between August 1997 and October 2003. $(^{210}\text{Pb})/(^{226}\text{Ra})_{\text{i}}$ are activity ratios age-corrected to 1 December 1993, the approximate collection date for NAUDUR samples, interpreted to be the latest possible eruption date for the youngest (N1) unit (see text). Both magnetic paleointensity and $(^{210}\text{Pb})/(^{226}\text{Ra})_{\text{i}}$ data for N1 and N2 units are consistent with ages of a few decades and suggest little time difference between the two. $(^{210}\text{Pb})/(^{226}\text{Ra})_{\text{i}}$ of ~ 1 for units T1 and T2 agree with magnetic paleointensity data suggesting ages considerably greater than 120 a.

3.2. Lava Ages

[29] The geological, geochemical, and age data indicate at least five separate eruptive episodes occurring over several hundred years in the area (Table 3 and Figure 7). The five geologic units identified clearly represent a minimum value for the number of eruptive episodes that have occurred over the timescale represented by our observations and samples. Because we have previously demonstrated that similar compositions can be erupted in separate eruptive episodes in this area [*Sinton et al.*, 2002], we cannot be positive that extrapolations based primarily on similar geochemistry alone constitute similar eruptive units. Furthermore, although our coverage is exceptional for mid-ocean ridge studies, we cannot be certain that all eruptive units have been identified and sampled and some smaller units could have been covered by later lava flows.

3.2.1. N1

[30] *Auzende et al.* [1994] argued that the N1 eruption must have concluded no more than a few months prior to their December 1993 visit, on the basis of water column turbidity, diffuse hydrothermal venting from biologically uncolonized areas of very fresh lava, sediment-free lava surfaces, and widespread presence of filamentous enteropneusts, bacteria and other vent biota. They also documented substantial changes in the axial region at 17°25'N requiring that most of the new

lava was emplaced after a 1984 *Cyana* study [*Renard et al.*, 1985]. Many of their observations are reminiscent of those following the eruption near 9°50'N on the EPR [*Haymon et al.*, 1993]. In 1994 [*Embley et al.*, 1998] saw changes to hydrothermal sites during submersible dives on N1 consistent with an evolving system that had not experienced subsequent volcanic activity, and independently estimated an eruption age of 2–3 a before late 1993 using hydrothermal fluid chemistry (e.g., ^3He , heat) and biological evidence. By the time of our 1999 program, diffuse hydrothermal activity venting warm water directly off of lava surfaces was no longer occurring and several focused flow hydrothermal sites, not yet developed in 1993, were in waning stages of activity. The collective observations suggest that the eruption was complete by December 1993. Paleomagnetic and $(^{210}\text{Pb}/^{226}\text{Ra})$ disequilibria data are consistent with these historical age estimates for the N1 flow; mean magnetic paleointensity values for three geographically dispersed samples overlap with the 1993 geomagnetic model value of 31.3 μT [*Bowles et al.*, 2005] (Table 3). Each of the 6 N1 samples analyzed has a $(^{210}\text{Pb}/^{226}\text{Ra}) < 1$, indicating that the magma feeding this eruption was significantly younger than 120 a.

3.2.2. N2

[31] N2 lava is clearly distinguishable from N1 by sediment cover, and subtle sediment differences observed on *Alvin* dives 3357 and 3360 imply a

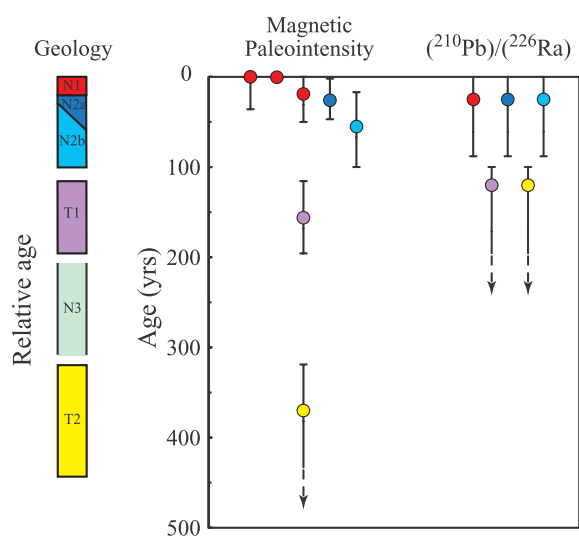


Figure 7. Graphical interpretation of lava ages based on geologic observations, magnetic paleointensity, and $(^{210}\text{Pb}/^{226}\text{Ra})$ disequilibria. Geologic observations constrain relative ages although an absolute age for the N1 group is further constrained by historical studies in the area (see text). Ages estimated from magnetic paleointensity and $(^{210}\text{Pb}/^{226}\text{Ra})$ data agree well with geologic observations. Paleointensity values for N1, N2a, and N2b are essentially indistinguishable from one another, but their absolute values reflect relative order as defined by geological observations. Measurable $(^{210}\text{Pb}/^{226}\text{Ra})$ disequilibria for N1, N2a, and N2b limit their ages to less than ~ 90 a and differences between the units to ~ 10 a. Error bars represent analytical uncertainties or limits of the technique. Magnetic paleointensity age estimates and $(^{210}\text{Pb}/^{226}\text{Ra})$ initial ratios are relative to 1993 A.D. and are also presented in Table 3.

slight age difference between N2a and N2b. $(^{210}\text{Pb}/^{226}\text{Ra})$ disequilibria values of three N2 samples overlap with those of N1, and two magnetic paleointensity values average $33.2 \mu\text{T}$, greater than the $30.3 \mu\text{T}$ mean for N1 lava but not outside of analytical error (Table 3 and Figure 7). Thus the combined magnetic paleointensity and $(^{210}\text{Pb}/^{226}\text{Ra})$ disequilibria results for N1 and N2 groups are essentially indistinguishable, suggesting that age differences are small and that N2 lava can be no more than a few decades older than N1.

3.2.3. T1

[32] T1 lava is demonstrably older than both the N1 lava and N2 group by superposition, sediment cover (Figure 2), and a single magnetic paleointensity value of $38.0 \mu\text{T}$. The latter suggests that the flow is ~ 160 a old [Bowles *et al.*, 2005]; a $(^{210}\text{Pb}/^{226}\text{Ra})$ activity ratio of ~ 1 is consistent with an age ≥ 120 a (Table 3 and Figure 7).

3.2.4. N3

[33] Contacts between N3 lava and T1 were not crossed by submersible, but sediment cover on N3 lava near $17^{\circ}34'\text{S}$ is much greater than on T1 lava farther north (Figure 2). Two N3 wax core samples occur directly down slope of T1 lava, also implying that N3 is older than T1. Similarly, no contacts between N3 lava and the oldest unit in the area (T2, Figure 1) were observed, but sediment cover is substantially less on N3 samples than on T2. Thus N3 lava is likely between ~ 160 and several hundred years old on the basis of magnetic paleointensity age estimates for lavas that geologically bracket N3 (T1 and T2).

3.2.5. T2

[34] All indications are that T2 is the oldest lava we have observed or sampled. Sediment is thickest on T2 (Figure 2) and a paleomagnetic intensity value of $45.1 \pm 1.7 \mu\text{T}$ (sample 3361-4) is substantially greater than other lavas from the region [Bowles *et al.*, 2005, Table 3]. The paleointensity age estimate of ~ 370 a is questionable because the paleomagnetic field model is poorly constrained prior to ~ 1840 A.D, but it is likely that this sample is at least 100 a, and possibly several hundred years older than T1 (~ 160 a). The $(^{210}\text{Pb}/^{226}\text{Ra})$ is ~ 1 , consistent with an age ≥ 120 a.

4. Discussion

4.1. Eruptive History

[35] The combined magnetic paleointensity and $(^{210}\text{Pb}/^{226}\text{Ra})$ disequilibria data quantify eruption frequency over the past several centuries. At face value magnetic paleointensity ages yield a ~ 75 a mean recurrence interval (i.e., five known episodes in ~ 370 a), yet there is clear evidence that these events were not separated equally in time. A very short time interval between N1 and N2 lavas is indicated by paleointensities, $(^{210}\text{Pb}/^{226}\text{Ra})$ disequilibria and sediment cover that nearly overlap between samples of the units. In contrast, larger differences in paleointensity and sediment cover data for T1 and T2 lava imply a much longer time between these two eruptions.

[36] Besides repose between major eruptive episodes, it is also important to consider that each unit could have been produced during multiple, small eruptive events, rather than single outpourings of lava. Sinton *et al.* [2002] described multiple flow units within the N1 compound flow field and we

described earlier that the N2 field may also comprise separate subunits. These observations are consistent with the hierarchy of eruptive phenomena on mid-ocean ridges, described from Iceland [Sæmundsson, 1991] and outlined by Sinton *et al.* [2002] in which flow fields produced during major eruptive episodes can contain the products of several individual eruptions.

[37] The roughly one decade we infer to separate N2 and N1 lava is in line with recurrence estimates of Perfit and Chadwick [1998], Macdonald [1998], and Sinton *et al.* [2002] for fast spreading ridges, and with observed eruption recurrence intervals on the northern EPR [Haymon *et al.*, 1993; Rubin *et al.*, 1994; Tolstoy *et al.*, 2006] and the CoAxial segment of the JdFR [Chadwick *et al.*, 1995; Embley *et al.*, 2000], but age constraints for older units suggest much greater repose times between eruptions. However, features such as large ridge cross-sectional area, shallow ridge depth, and a shallow magma reservoir reflector indicate that a high magmatic budget has characterized this area for a period much longer than the few decades over which we have documented closely spaced eruptions. Thus, if eruptions occur roughly every decade on the SEPR, there should have been tens of them in the past several hundred years and we have distinguished only five, leaving open the possibility that we may have combined products of multiple episodes into our individual units. However, the distinct contacts and age contrasts among the identified units suggest instead that eruptive activity in this area has been uneven and highly episodic over the last few hundred years, such that a single “recurrence interval” does not apply even along this very robust section of a very fast spreading ridge; eruptive activity, at ridges with lower magma supply might be expected to be even more so.

[38] The combined total estimated minimum volume of the N1, N2, and T1 flow fields is $<0.5 \text{ km}^3$ (0.14 km^3 , 0.2 km^3 , and 0.05 km^3 , respectively, based on mapped areas and thicknesses estimated from depths of collapse pits and flow front heights). This value is less than half of the volume of the upper crust produced for this $\sim 30 \text{ km}$ of ridge in the last $\sim 160 \text{ a}$ assuming an average layer 2 thickness of 1.3 km and a full spreading rate of 146 mm/a . This result is consistent with deformation studies of the Krafla rifting event in Iceland [Tryggvason, 1984, 1986; Sigurdsson, 1987] and geologic observations at Hess Deep [Stewart *et al.*, 2005] implying that less than half of the magma that exits shallow reservoirs as dikes during rifting

episodes along mid-ocean ridges is ever erupted on the surface.

4.2. Conditions of Magmatic Differentiation

[39] Although the trace element and isotopic data discussed previously require multiple primary magmas at this part of the SEPR, major element trends indicate that magmatic differentiation also plays an important role in their compositional diversity. TiO_2 , FeO^* , Na_2O , K_2O , and P_2O_5 increase with decreasing MgO along subparallel trends in each of the geologic units that show a substantial range of MgO contents (Figure 3). Plagioclase and olivine fractionation cause Al_2O_3 to decrease steadily with decreasing MgO. The inflection in $\text{CaO}/\text{Al}_2\text{O}_3$ versus MgO marks the onset of Ca-rich clinopyroxene (CPX) fractionation at $\sim 7.9 \text{ wt\% MgO}$ for N1 and N3 lavas; there is greater $\text{CaO}/\text{Al}_2\text{O}_3$ range below 8.0 wt\% MgO in N2 lava but the same inflection is apparent. A positive $\text{CaO}/\text{Al}_2\text{O}_3$ versus MgO correlation in T1 lava also indicates CPX fractionation but the point where this began is undetermined due to lack of high-MgO samples in this unit. Limited compositional variance and small sample numbers make it difficult to determine if the T2 magma experienced varying degrees of fractional crystallization.

[40] Major element variations for all groups are well simulated using MELTS [Ghiorsso and Sack, 1995] with conditions of $\sim 0.5 \text{ kbar}$ total pressure, H_2O contents of $0.1\text{--}0.3 \text{ wt\%}$, and $f\text{O}_2 = \text{QFM}-2$, consistent with evolution in a magma reservoir $\sim 1.5 \text{ km}$ below the seafloor (Figure 3), which broadly corresponds to the AMC reflector depth in the area [Detrick *et al.* 1993]. Different parental melts are required for the N-MORB and T2 groups, but the same shallow crustal differentiation conditions apply.

4.3. Geochemical Evidence for Magma Mixing in the AMC

[41] Geochemical variations in all three N-MORB groups require mixing of compositionally distinct parental magmas. There is a nearly linear correlation among N1 samples between MgO and $^{206}\text{Pb}/^{204}\text{Pb}$, Th/U and Sr concentration, at nearly constant Zr/Y (Figure 5). Because Pb isotope and Th/U ratios are little affected by melting and differentiation processes, these variations primarily reflect compositional differences in the mantle source. The trends for Zr/Y and Sr cannot be modeled by fractional crystallization at the con-

ditions of Figure 3 using published distribution coefficients (Figure 5). These relations can be explained by simple mixing between a high-MgO magma with high $^{206}\text{Pb}/^{204}\text{Pb}$, Th/U (≥ 18.80 and ≥ 2.84 , respectively), Zr/Y and Sr content and a cooler, lower-MgO magma with substantially lower $^{206}\text{Pb}/^{204}\text{Pb}$, Th/U ratios (≤ 18.68 and ≤ 2.45), Zr/Y and Sr. Both compositional subgroups of N2 lava show the same general correlation of $^{206}\text{Pb}/^{204}\text{Pb}$, Th/U, Zr/Y and Sr concentrations with MgO as does N1 (Figure 5). Elevated Th and U concentrations and Zr/Y ratios in N2b lava can be explained by mixing between N2a and older T1 magma. Trace element trends for three N3 samples generally mimic, but are offset from, those of the N1 and N2 groups, suggesting that magma mixing also has contributed to the compositional diversity of this group.

[42] The evidence for magma mixing in T1 and T2 lava is less clear than for the two youngest groups, partly because T1 and T2 have fewer isotope and trace element analyses. T1 lava is the most compositionally homogeneous magma group but shows as much Nb/Er and La/Ce variation as N1 and N2 lavas (Figure 4).

[43] To summarize, the three N-MORB groups all show evidence of mixing between lower-temperature, more incompatible element-depleted melts and less differentiated magmas that are relatively more enriched in incompatible trace elements and Pb isotopic composition; T-MORB groups are heterogeneous with respect to major and/or trace elements but it is unclear if magma mixing has contributed to their diversity.

[44] The strong correlations between MgO and isotopic or trace element indicators of mantle-derived magma compositions are consistent with the mixing primarily taking place in shallow magma reservoirs. Magmatic evolution deeper in the crust or upper mantle will have little effect on MgO contents because of strong buffering by high-temperature phases and conditions in those regions [e.g., *Sinton and Detrick*, 1992]. Thus, if mixing of two compositional end-members had occurred deeper in the magmatic system while both were still relatively undifferentiated, it would be a remarkable coincidence that the isotope- and trace element-depleted parts of the mixture always cooled to a greater degree. It is more likely that for each N-MORB group, incompatible element-depleted magma resided in the shallow AMC where it variably cooled and differentiated to lower MgO. Recharge subsequently introduced hotter,

but more incompatible element-enriched magma into the AMC, followed by variable mixing between the two.

[45] Although most major element differentiation trends are nearly linear and difficult to distinguish from simple mixing lines, CaO/Al₂O₃ versus MgO (Figure 3) trends preserve the previously discussed CPX inflection, which would not be preserved if high-MgO (and high-CaO/Al₂O₃) recharge magma was uniformly mixed with a wide range of differentiated magmas. There are, however, relatively few N-MORB samples with <7.9 wt% MgO; these cool parts of the AMC between 17°24.4'S and 17°27.9'S must have received little replenishment with new, hotter magma, leaving those parts of the liquid lines of descent relatively unaffected by mixing. An increasing ratio of new to resident magma produces the bulk of the data plotting at or above 7.8 wt% MgO. By this process major element trends generally consistent with shallow-level differentiation are preserved with an overprint of isotopic and trace element indicators of mixing between incompatible element-depleted and relatively enriched magmas.

[46] Compositional variations within N1 also allow us to evaluate the geometry of magma recharge in this area. Although isotope and Th/U ratios within N1 correlate well with MgO, they do not vary regularly along axis. If new magma was introduced to the reservoir near 17°30'S where MgO reaches a maximum, variable mixing with resident magma to the north should produce an along-axis gradient in composition that essentially mimics the trend observed versus MgO. Instead, the lack of systematic compositional variation with latitude requires that newer magma was introduced to the shallow reservoir at a range of locations along axis and mixed to different extents with preexisting magma prior to eruption. Additionally, the efficacy of mixing along-axis is likely to be limited by the high aspect ratio of the AMC.

[47] It has recently been demonstrated that average low-MgO MORB from fast spreading ridge segments tend to be more homogeneous with respect to mantle-derived characteristics than those at slower rates, because magma homogenization and low-pressure differentiation are promoted by high melt supply to the crust [*Rubin and Sinton*, 2007]. It is therefore instructive to consider how incompletely mixed magmas within single eruptions as documented here provide additional constraint on the operative processes. $^{87}\text{Sr}/^{86}\text{Sr}$ ranges by ± 0.00002 among N1 lavas, roughly 7% of the

range in axial MORB from 13–18°S [Mahoney *et al.*, 1994]. Abundant near-axis seamounts in this area show an even greater range of isotopic and incompatible trace element ratios than do the along-axis samples [Hall *et al.*, 2006; Mahoney *et al.*, 1994; Niu *et al.*, 1996]. Although sampling differences limit the utility of comparisons between samples from one eruption and samples from many eruptions, these results further suggest that magma mixing and homogenization in the AMC have substantially reduced, but not eliminated, geochemical evidence for multiple parental magmas over short temporal and spatial scales.

4.4. Thermal Structure of the Shallow Crust

[48] An interesting feature of N1 lava is the striking change in eruptive characteristics and lava composition north and south of 17°29–30'S (Figure 8). To the north high eruptive volumes and average eruption rates are associated with low MgO contents, whereas the opposite is true to the south. The volcanological evidence (i.e., well-developed en echelon eruptive fissures, high effusion rate flow morphologies, well-developed lava channels and tube systems distributing lava off axis, and overall erupted volume) all suggest the primary eruptive center was located near 17°27'S. Thus either the eruption was focused 8–9 km north of the highest-temperature subaxial magma, as indicated by lava MgO content or, alternatively, significant differentiation accompanied intrusion and transport of magma to the north during the eruption. Because of short timescales involved in the latter scenario, one might expect disequilibrium between lava composition and entrained crystals, which can be evaluated with mineral compositions in N1 lava.

4.4.1. N1 Olivine Data

[49] Olivine phenocrysts were analyzed in seven N1 samples chosen to represent the full compositional and geographic range of the flow field. Using a distribution coefficient for Fe and Mg partitioning between olivine and melt of 0.3 ± 0.03 [Roeder and Emslie, 1970; Ulmer, 1989], a typical MORB $\text{Fe}^{3+}/\text{total Fe}$ ratio of 0.1 ± 0.03 [Christie *et al.*, 1986; Bézou and Humler, 2005], and glass and olivine compositions, we determined that N1 mean olivine compositions are in equilibrium with coexisting melt (Figure 9) over the range of N1 MgO contents.

[50] Along-axis variations in olivine composition generally mimic along-axis variations in MgO contents, i.e., high Fo olivines occur in the southern part of the flow field and lower Fo olivines occur farther north. The presence of equilibrium olivine over a range of MgO contents is not consistent with differentiation accompanying dike intrusion and transport to the surface, which presumably occurs over a few hours to days. Rather, we interpret the equilibrium olivine to reflect somewhat longer term variations within the AMC prior to eruption. Although the range of MgO within N1 glass indicates considerable olivine (and some CPX) crystallization, most N1 lava samples have <1% total phenocrysts, indicating that crystal fractionation processes are efficient and that the few N1 olivines that are present represent recently crystallized grains that post date mixing between high- and lower-MgO magma.

4.4.2. Relationships Between Lava Composition, Eruptive Phenomena, and Pre-eruptive Magma Temperature

[51] Above we argued that eruption of the N1 unit occurred from a magma chamber with significant internal chemical heterogeneity and focused 8–9 km north of the highest-temperature subaxial magma. Although this result is perhaps counterintuitive, we are not aware of any previous studies that relate erupted volumes or other volcanological phenomena to subaxial magma temperatures in moderately long fissure eruptions underlain by quasi-continuous magma reservoirs.

[52] Variations in MgO along-axis correlate crudely with depth to the seismic reflector commonly interpreted to be the top of the AMC (Figure 8). Shallowest at ~17°25'S, ~800 mbsf (meters below seafloor), the seismic reflector deepens steadily to the north to ~1400 mbsf at 17°22'S, and more gradually to the south to a similar depth at ~17°32.5'S [Detrick *et al.*, 1993; Hooft *et al.*, 1997]. South of 17°32.5'S to the end of the study area at 17°36'S, the depth to the reflector varies between 1250 and 1350 mbsf. The lowest-temperature samples are from sites located either directly over or slightly south of the shallowest portion of the AMC, the highest-temperature samples were collected south of 17°30'S where the AMC is 400–600 m deeper. Thus the eruption center for N1 lava is near the location of the shallowest magma, but not the location of the hottest magma. A similar correlation of high-MgO lava with greater AMC depth along the Cleft segment of the JdFR is

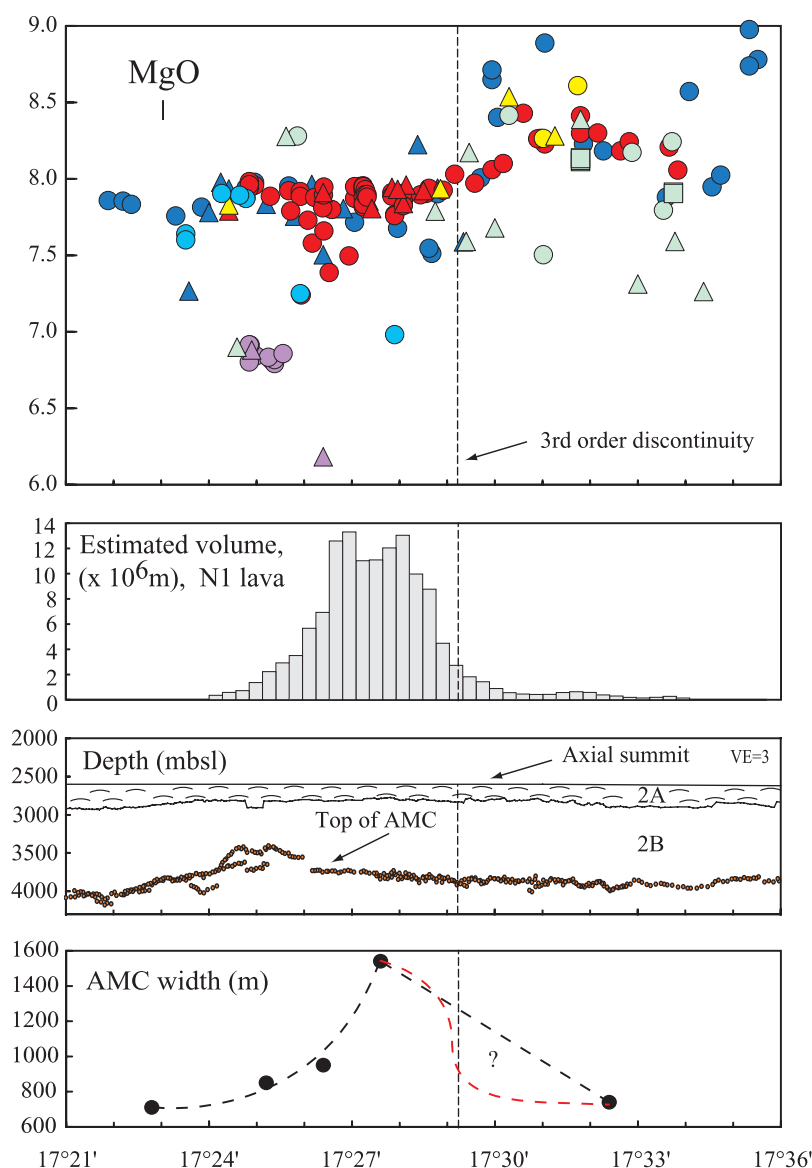


Figure 8. MgO content, estimated volume of N1 lava per 500 m of latitude, AMC profile, and AMC width versus latitude. Similar MgO variations versus latitude indicate that the location of hottest and coolest magma has persisted for several eruptive cycles. High-temperature (high-MgO) lava has mainly been erupted south of the third-order discontinuity at $\sim 17^{\circ}29.2'S$, where the depth to the axial magma reservoir is greater. Volume estimates, derived by multiplying flow field area (500 m bins) with estimated thicknesses from geologic observations such as collapse pit depths, flow front heights, and kipuka, indicate that most of the volume of N1 lava erupted between $\sim 17^{\circ}26'S$ and $17^{\circ}29.2'S$, where the flow field is widest and collapse pits locally are up to 12 m deep. It is notable that this region overlies a relatively low-temperature part of the magma reservoir. Much lower volumes were erupted from the deeper, hotter AMC south of $17^{\circ}29.2'S$.

alluded to by *Stakes et al.* [2006], and demonstrated regionally for the five segments that make up the JdFR by *Rubin and Sinton* [2007].

[53] These observations have important implications for processes that control the residence depth of axial magma chambers and the extent of differentiation that occurs within them. Because most SEPR magmas are multiply saturated with olivine

and plagioclase, temperature should bear an inverse relationship to density [e.g., *Stolper and Walker*, 1980; *Sparks et al.*, 1980], and buoyancy considerations therefore predict that the hottest magma should rise to shallower levels in the crust. However, *Hooft and Detrick* [1993] showed that most mid-ocean ridge magmas are thermally compensated at depths below their level of neutral

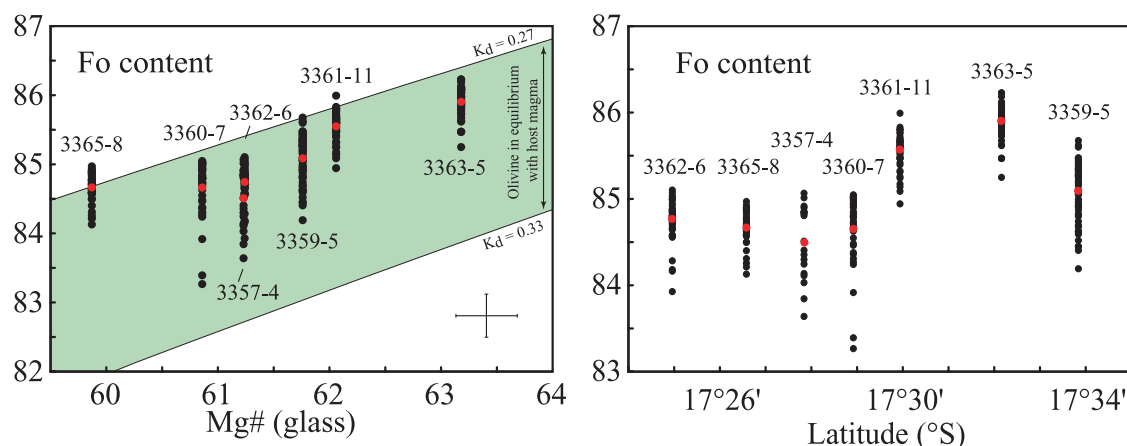


Figure 9. Olivine compositions versus glass Mg# and latitude for N1 samples. Black circles represent individual olivine analyses; red circles are average Fo contents for each sample; green region shows the range of olivine compositions in equilibrium with their host magma based on *Roeder and Emslie* [1970] and *Ulmer* [1989]. Olivine compositions are mainly in equilibrium with their host magmas and generally mimic the along-axis distribution of high- and low-MgO samples in N1 lava. These data suggest that the major element compositional variation observed in lavas collected at the surface likely reflects that of the subaxial magma reservoir prior to eruption. Complete olivine composition data are available as auxiliary material Table S3.

buoyancy, and that temperature structure is more important than buoyancy in controlling magma depth. The eruption of the lowest-temperature lavas from the shallowest parts of the AMC suggests that extent of shallow-level cooling may be an important control on magma temperature. The most efficient mechanism of heat removal is hydrothermal cooling, and it is notable that there are many hydrothermal sites, both low- and high-temperature, clustered between 17°24'S and 17°28.5'S (Figure 1). Cooling is most effective in the shallowest part of the crust, closest to the seawater interface and where porosity is high. The along-axis thickness of seismic layer 2A is relatively constant in this area [*Hoofst et al.*, 1997], so the thickness of layer 2B, with higher seismic velocity and presumably less porosity, must correlate with AMC depth, i.e., be thinnest where the AMC is shallowest (Figure 8). The association of the lowest-temperature magma with high layer 2A/2B thickness ratio and higher average porosity supports the contention for a relationship between magma temperature and hydrothermal cooling. Because temperature should increase with depth, it appears that magma reservoirs in this area adjust to the ambient temperature of the crustal level where they reside, rather than control it. A similar relationship and interpretation for global MORB has recently been determined by *Rubin and Sinton* [2007].

[54] Although the relationship between reservoir depth and magma temperature reflect hydrothermal

cooling efficiency changes with depth, this does not explain the ultimate control on where in the crust magma becomes compensated; i.e., the residence depth for a quasi-steady state magma reservoir. Another important factor is the overall magma supply rate because the magma compensation depth in the crust involves a balance between magma supply from below and cooling from above. Cooling from above will tend to increase AMC depth within the crust, whereas magma supply will tend to decrease it. The highest magma supply to the axial region is likely to be where the AMC is shallowest and widest; i.e., near 17°25'–27'S (Figure 8). Because the crust above the AMC is thinnest there, it is the most likely place for eruptions to be initiated because magma driving pressures required to initiate upward dike propagation are directly related to dike height [*Rubin*, 1993]. Although we do not know where the N1 eruption initiated, it is clear that the main locus of eruptive activity was concentrated between 17°26'S and 17°28'S, where magma temperatures and AMC depth are relatively low.

[55] A compilation of all data for the area indicates that the along-axis location of hottest and coolest magma is not unique to the N1 eruption but may have persisted for several eruptive cycles. The highest MgO samples occur between 17°30'S and 17°35.3'S in each of the magmatic units, whereas the lowest occur between 17°24.4'S and 17°27.9'S (Figure 8). With the exception of N3 lava, there is little overlap of high and low MgO samples north

and south of 17°30'S (only one sample with MgO >8.06 wt% occurs north of the boundary and three samples with <8.06 wt% MgO are present south of it, all from the N2 group). T1 lava is spatially restricted to the region above the shallowest portion of the AMC between 17°23.6'S and 17°26.4'S, and this group has the lowest MgO of any in the area. It is unknown whether T1 lava erupted only from the shallow portion of the magma reservoir or if T1 lava erupted elsewhere along the ridge and was subsequently covered more recent lavas. Similarly six T2 samples show a temperature distribution crudely similar to the more populous and (apparently) geographically extensive lava types. Although the lowest and highest MgO samples within N3 lava occur at 17°24.6'S and 17°30.3'S respectively, geographic distribution of MgO is relatively uniform in the group as a whole. The average MgO content of all samples south and north of 17°30'S is 8.20 wt% and 7.71 wt%, respectively; MELTS-derived liquidus temperatures yield a temperature difference of ~9°C (1195°C–1186°C). These observations suggest that the shallow region in the AMC has existed for at least ~160 a, and possibly for more than 300 a.

4.5. The 17°29'S Discontinuity

[56] Primarily on the basis of bathymetric data, *White et al.* [2000] identified a left-stepping, non-overlapping third-order segment boundary at ~17°29.2'S (Figure 1) that corresponds to the transition zone between high- and low-MgO samples along-axis (Figure 8). These workers suggested that such discontinuities reflect breaks in the subaxial magmatic plumbing system. It is apparent in Figure 1 that the near-axis region is broader to the north and narrower to the south of the discontinuity. The substantial difference in axial morphology to the south and north of 17°29'S probably reflects at least several hundred years of crustal construction, because outward bends in the bathymetric contours can be seen extending several km away from the present axis to depths of at least 2700 m (Figure 1).

[57] A break in the AMC is not apparent in the seismic reflection data, although it is apparent that the AMC is wider as well as slightly shallower north of the discontinuity and narrows dramatically south of it (Figure 8). Thus the change in MgO content (temperature) across the discontinuity can be understood in terms of the previously discussed scenario for mixing of cooler, resident melts with

new, hotter recharge melts along axis. The MgO of a magma mixture reflects the relative volumes and temperatures of the mixing components. Because the amount of differentiated magma residing in the AMC should be significantly less in the south than to the north, uniform recharge of hot magma arriving at the AMC will be less diluted by low-temperature resident magma in the narrow, lower volume southern part, and the change in MgO across the boundary at 17°29'S is thus accounted for by a discontinuity in magma volume prior to recharge.

[58] The eruptive fissures of the N1 eruption appear not to have been affected greatly by longer-lived segmentation of the axis. Although N1 eruptive fissures are topographically centered on the axis in the north, they continue to the south at least 9 km past the discontinuity on the western side of the topographic axis, which is displaced ~280 m eastward south of the discontinuity (Figure 1). The 280-m eastward step in the topographic axis is less than the average width of the AMC in this area (Figure 8), so these fissures also presumably overlie eruptible magma. If the eruption was centered in the north, as we argued above, the dikes appear to have propagated across the boundary without disruption, indicating that local stresses in the shallow crust were not significantly different north and south of 17°29'S.

4.6. Magma Transport From Subaxial Reservoirs

[59] The relationships between MgO, AMC depth and the location of a third-order segment boundary are most easily explained if magma transport through dikes from magma reservoir to seafloor is primarily vertical. Of particular importance is the coincidence of the sudden increase in MgO south of 17°29'S; significant along-axis transport of magma either to the north or south should smear out or geographically displace this relationship. That surface lava compositions preserve an apparently faithful "snapshot" of the underlying magma reservoir implies that magma cannot have migrated laterally more than ~1.5 km from the AMC to the eruption site, a conclusion that applies to all magma groups except N3. Similarly, the coincidence of a boundary between intragrabens lavas of two distinct compositions with a vertical offset in the AMC near 18°33'S [*Sinton et al.*, 2002] also is consistent with vertical rise of magma directly with lateral migration of no more than a few hundred meters. Thus, in two relatively well-documented

cases along the SEPR, relationships between erupted lava compositions and subaxial magma reservoirs seem to require predominantly vertical ascent of magma from the AMC to the seafloor.

[60] This result is perhaps surprising given the up to 60 km of along-axis migrations in seismicity that have been documented at Krafla in Iceland [Einarsson and Brandsdóttir, 1980], along the JdFR [Dziak *et al.*, 1995], and at Kīlauea, Hawai'i [Koyanagi *et al.*, 1987], and occur in each seismically detected eruption of the JdFR and Gorda Ridges [Dziak *et al.*, 2007]. Reconciliation of our observations, which appear to require near-vertical magma transport, with evidence for laterally migrating seismicity in other volcanic systems, can be accommodated in two ways. First, vertical magma transport within dikes and lateral seismic propagation are not necessarily mutually exclusive. For example, magma may begin to rise vertically above the point of initial dike intrusion while cracking in the crust might propagate laterally, progressively tapping magma along the top of a continuous reservoir; most factors affecting stress intensity around dikes favor upward growth and eruption rather than lateral growth [Rubin and Pollard, 1987].

[61] Another possibility is that true lateral dikeing, i.e., along axis transport of magma in dikes, does indeed occur elsewhere, particularly where magma accumulation along axis is more episodic, but perhaps not for the SEPR eruptive units in this study. Studies of flow direction in dikes at Krafla in Iceland, at Ko'olau volcano in Hawai'i, and in the Troodos ophiolite suggest that magma transport in dikes includes both near-horizontal and near-vertical components of flow [Sigurdsson and Sparks, 1978; Knight and Walker, 1988; Staudigel *et al.*, 1992; 1999; Varga *et al.*, 1998; Borradaile and Gauthier, 2006]. However, for the Krafla and Ko'olau cases, those dikes are thought to emanate from a centrally focused magmatic source, where lateral flow is required to transport magma to distal portions of the volcanic system. These relatively deep, centralized magmatic supply systems may not be good analogs for fast spreading mid-ocean ridges underlain by shallow, nearly continuous lenses of eruptible magma [Sinton and Detrick, 1992]. In contrast, magnetic fabrics in dikes of the Oman ophiolite show an overall tendency for vertical flow [Rochette *et al.*, 1991].

[62] At least one geological factor may potentially make near-vertical dike transport more likely at 17°30'S on the SEPR than elsewhere along the

mid-ocean ridge system. The average depth to the AMC is ~1.3 km below the seafloor and rises to <1 km at 17°26'S, substantially shallower than along the northern EPR (~1.6 km) [Detrick *et al.*, 1993] and most other mid-ocean ridge systems. Rubin and Pollard [1987] showed that the proximity of a free surface, e.g., the seafloor, will tend to increase dike height relative to length. Thus the shallow AMC in this area may allow dikes to intersect the seafloor close to their point of origin without substantial along-axis magma transport. The juxtaposition of variable lava compositions in our area can be explained by rapidly evolving conditions in the near subsurface, and near-vertical dike transport, making it unnecessary to call upon substantial along-axis transport from distant, chemically distinct magma reservoirs as suggested by Stewart *et al.* [2005].

4.7. Temporal Magmatic Evolution of the Area

[63] The SEPR 17°30'S area is characterized by rapid variations in parental magma compositions over the last few hundred years, requiring different source compositions and melting extents. Although radiogenic isotopes track variations in source composition relatively unambiguously, it is much less straight forward to infer melting conditions. The latter usually relies on both major element and incompatible element compositions and ratios. Yet, there is evidence for a decoupling between radiogenic isotopes and incompatible elements in N-MORB from along the SEPR from 13° to 23°S that occurs as a long wavelength feature [Sinton *et al.*, 1991; Mahoney *et al.*, 1994]. Superposed on the N-MORB gradients is an irregular distribution of T-MORB that all previous workers have interpreted to represent low degree melts [Sinton *et al.*, 1991; Mahoney *et al.*, 1994; Niu *et al.*, 1996; Hall *et al.*, 2006]. Our data also suggest that T-MORB and N-MORB units in this area are derived from lower and greater extents of partial melting, respectively. T2 lava has relatively unradiogenic isotopic compositions and substantially higher Na₂O, K₂O, and P₂O₅ than the other magma types. In contrast, T1 lavas are only slightly enriched in incompatible elements, even accounting for the more extreme amount of differentiation, but have isotopic compositions in the middle of the spectrum of lavas represented here. Aspects of T1 major element composition are consistent with derivation from primitive N-MORB melts (Figure 3), yet elevated K₂O concentrations and greater highly incompatible to moderately incom-

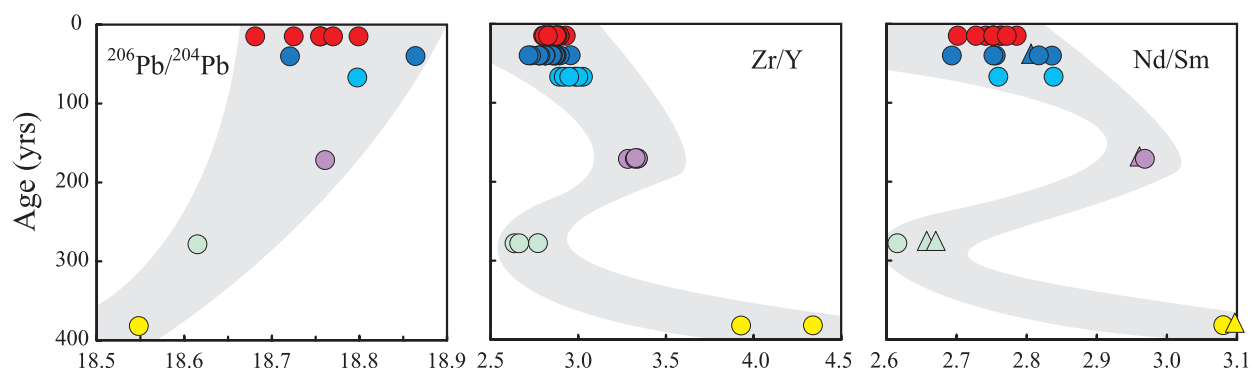


Figure 10. Pb isotope and trace element ratios versus time show geochemical evolution of the area over the last several hundred years. The oldest unit has the lowest $^{206}\text{Pb}/^{204}\text{Pb}$, indicating derivation from a source with long-term, relatively low U/Pb. Younger units have been derived from a progressively more radiogenic source. Incompatible trace element ratios indicate a more complicated pattern, requiring either recent variations in source composition or, more likely, significant variations in extent of melting in the last few hundred years. See text for discussion.

patible trace element ratios (Figure 4) suggest that it may also be derived from lower degrees of partial melting.

[64] Using Pb isotopic composition as a proxy for source composition and highly to moderately incompatible element trace element ratios (e.g., Zr/Y, Nd/Sm) as inverse proxies for degree of melting we can track how source composition and melting processes have varied over the last few hundred years (Figure 10). Note that our data indicate that these processes have operated more or less independently, i.e., there is no apparent relation between mantle source composition and extent of melting.

[65] Overall, radiogenic isotopic compositions generally trend from less to more radiogenic Sr and Pb over the last several hundred years. The oldest unit, T2, has Pb and Nd isotopic compositions similar to 17° – $17^{\circ}30'$ SEPR lavas [Mahoney *et al.*, 1994], although $^{87}\text{Sr}/^{86}\text{Sr}$ (0.70256) is substantially lower than other samples along this broad axial isotopic peak (~ 0.7027). Isotope composition changed to more radiogenic Pb and Sr values with N3, T1, and N2b lava, reflecting input of magma derived from a mantle source with higher time-integrated parent-daughter ratios (Figure 10). In fact, lavas produced over the last ~ 160 a (T1, N2, and N1) include the most radiogenic Pb and Sr isotopic signatures yet recorded along the SEPR axis, reaching values previously observed only in off-axis seamounts [Niu *et al.*, 1996; Hall *et al.*, 2006]. Although just one sample from each of the magma types T2 through N2a has been analyzed for isotopes, it is likely that isotopic diversity exists within those groups because trace element variations mimic those of the isotopically variable N2a and N1 lavas.

[66] The evolution of incompatible trace element ratios suggests variations in melting extents that are much more irregular and temporally variable than the more steady change in source composition indicated by radiogenic isotopes. Although previous studies also have argued for decoupling between source compositions and melting extents [Niu *et al.*, 1996; Hall *et al.*, 2006] those studies were conducted on off-axis samples where upwelling is expected to be more variable than beneath the spreading axis. A thorough evaluation of the melting processes contributing to chemical heterogeneity in this area is beyond the scope of the present paper and will be addressed in a later contribution.

[67] It is notable that every eruptive unit in this area is associated with a distinct parental magma composition inherited from mantle processes. Thus both the temporal variation in mantle melting processes and the rate of supply of magma to the crust must occur over timescales at least as high as the eruption recurrence rate. Although recharge of mantle-derived magma might be expected to be episodic beneath many mid-ocean ridge systems, we conclude that recharge at this very fast spreading ridge is essentially continuous at the scale of tens to hundreds of years, which is the resolution afforded by volcanic eruptions in this area.

5. Conclusions

[68] 1. High magma production rates and frequent tapping of magma reservoirs has produced at least five separate flow fields over the last several hundred years in a region of very high spreading rate; each of these flow fields probably represents a

major rifting event. Individual units exhibit a diverse range of lava compositions. Geological observations, magnetic paleointensity and ($^{210}\text{Pb}/^{226}\text{Ra}$) disequilibria age data give mutually consistent ages, and indicate highly intermittent eruptive activity even along this very robust section of ridge.

[69] 2. This region is characterized by lavas with relatively high isotopic and chemical diversity. Three magmatic groups show isotopic and/or trace element variations that require mixing between chemically and isotopically distinct, high-temperature parental melts with magma that has undergone varying degrees of magmatic differentiation. Major and trace element systematics and MELTS crystallization simulations suggest that mixing and differentiation processes occurred at a pressure of ~ 500 bars, consistent with the depth (≤ 1400 mbsf) to the top of the AMC. The lack of systematic mixing trends with latitude suggests that new magma is intruded and mixed with resident magma along the length of the AMC, and not from widely separated, focused injection centers.

[70] 3. MgO contents and pre-eruptive magma temperatures correlate crudely with depth to the top of the magma reservoir, suggesting that a temperature-depth relationship exists for magma residing in the AMC. AMC depth appears to be controlled by a delicate balance of magma supply from below and cooling (largely hydrothermal) from above, i.e., the coolest lavas appear to erupt from the shallowest and widest parts of the AMC. Geographic trends in most of the lava units are the same, suggesting that the along-axis temperature distribution in the AMC has existed for at least ~ 160 a. A distinct change in MgO content across an axial discontinuity and AMC width discontinuity at $17^\circ 29.2'\text{S}$ implies that newly arrived, hotter magma is less diluted by resident magma on the narrower, southern side of the discontinuity, a conclusion that also argues for relatively uniform, rather than focused, recharge along-axis.

[71] 4. Correlations among surface lava compositions, a third-order segment boundary at $17^\circ 29.2'\text{S}$, and depth and width of the directly underlying AMC suggest that magma transport in this region is primarily vertical; lateral transport in dikes appears to be limited to less than a few kilometers. The lack of evidence for significant lateral dike propagation in this region may reflect the very shallow magma reservoir that is present at this very high spreading rate. We therefore interpret highly variable surface lava compositions in terms of rapidly changing magma compositions in the

underlying shallow magma reservoir, and not a result of significant along-axis transport through dikes from distal parts of the AMC.

[72] 5. Isotopic and trace element variations within and between lava units, coupled to moderately high resolution dating, indicate a progressively changing mantle source, complicated by short-term variations in extent of melting. Each of the last five erupted units is distinct with respect to mantle-derived chemical characteristics. This observation requires that changes in mantle melting processes in this region occur at rates that are less than the eruption rate.

Acknowledgments

[73] This work was supported by National Science Foundation grants OCE96-33398 and OCE02-41578. The manuscript benefited greatly from careful reviews by Mike Perfit, Dave Christie, Julie Bowles, John Mahoney, and associate editor Damon Teagle. We thank Doug Pyle, Sarah Cook, Chuck Fraley, John Mahoney, Kent Ross, JoAnn Sinton, and Cliff Todd for help with sample preparation and/or chemical analyses. This is SOEST contribution 7171.

References

- Auzende, J. M., V. Ballu, R. Batiza, D. Bideau, M. H. Cormier, Y. Fouquet, P. Geistdoerfer, Y. Lagabriele, J. Sinton, and P. Spadea (1994), Present-day magmatic, tectonic and hydrothermal activity on the East Pacific Rise between 17°S and 19°S (Naudur Cruise), *C. R. Acad. Sci., Ser. II*, 319, 811–818.
- Auzende, J. M., et al. (1996), Recent tectonic, magmatic, and hydrothermal activity on the East Pacific Rise between 17°S and 19°S : Submersible observations, *J. Geophys. Res.*, 101, 17,995–18,010.
- Bach, W., E. Hegner, E. Erzinger, and M. Satir (1994), Chemical and isotopic variations along the superfast spreading East Pacific Rise from 6° to 30°S , *Contrib. Mineral. Petrol.*, 116, 365–380.
- Beattie, P., C. Ford, and D. Russell (1993), Partition coefficients for olivine-melt and orthopyroxene-melt systems, *Contrib. Mineral. Petrol.*, 109(2), 212–224.
- Bézos, A., and E. Humler (2005), The $\text{Fe}^{3+}/\Sigma\text{Fe}$ ratios of MORB glasses and their implications for mantle melting, *Geochim. Cosmochim. Acta*, 69, 711–725, doi:10.1016/j.gca.2004.07.026.
- Bindeman, I. N., A. M. Davis, and M. J. Drake (1998), Ion microprobe study of plagioclase-basalt partition experiments at natural concentration levels of trace elements, *Geochim. Cosmochim. Acta*, 62, 1175–1193.
- Borradaile, G. J., and D. Gauthier (2006), Magnetic studies of magma-supply and sea-floor metamorphism: Troodos ophiolite dikes, *Tectonophysics*, 418, 75–92.
- Bowles, J., J. S. Gee, D. V. Kent, E. Bergmanis, and J. Sinton (2005), Cooling rate effects on paleointensity estimates in submarine basaltic glass and implications for dating young flows, *Geochim. Geophys. Geosyst.*, 6, Q07002, doi:10.1029/2004GC000900.

- Bowles, J., J. S. Gee, D. V. Kent, M. R. Perfit, S. A. Soule, and D. J. Fornari (2006), Paleointensity applications to timing and extent of eruptive activity, 9°–10°N East Pacific Rise, *Geochem. Geophys. Geosyst.*, **7**, Q06006, doi:10.1029/2005GC001141.
- Carlut, J., and D. V. Kent (2000), Paleointensity record in zero-age submarine basalt glasses: Testing a new dating technique for recent MORBs, *Earth Planet. Sci. Lett.*, **183**, 389–401.
- Carlut, J., M.-H. Cormier, D. V. Kent, K. E. Donnelly, and C. H. Langmuir (2004), Timing of volcanism along the northern East Pacific Rise based on paleointensity experiments on basaltic glasses, *J. Geophys. Res.*, **109**, B04104, doi:10.1029/2003JB002672.
- Chadwick, W. W., Jr., R. W. Embley, and C. G. Fox (1995), SeaBeam depth changes associated with recent lava flows, CoAxial segment, Juan de Fuca Ridge: Evidence for multiple eruptions between 1981–1993, *Geophys. Res. Lett.*, **22**(2), 167–170.
- Chappell, B. W. (1991), Trace element analysis of rocks by x-ray spectrometry, *Adv. X-Ray Anal.*, **34**, 263–276.
- Christie, D. M., I. S. E. Carmichael, and C. H. Langmuir (1986), Oxidation states of mid-ocean ridge basalt glasses, *Earth Planet. Sci. Lett.*, **79**, 397–411.
- Cormier, M.-H., K. C. Macdonald, and D. S. Wilson (1995), A three-dimensional gravity analysis of the East Pacific rise from 18° to 21°30'S, *J. Geophys. Res.*, **100**(B5), 8063–8082.
- Detrick, R. S., A. J. Harding, G. M. Kent, J. A. Orcutt, J. C. Mutter, and P. Buhl (1993), Seismic structure of the southern East Pacific Rise, *Science*, **259**, 499–503.
- Dziak, R. P., C. G. Fox, and A. E. Schreiner (1995), The June–July 1993 seismo-acoustic event at CoAxial segment, Juan de Fuca Ridge: Evidence for a lateral dike injection, *Geophys. Res. Lett.*, **22**(2), 135–138.
- Dziak, R. P., D. R. Bohnenstiehl, J. P. Cowen, E. T. Baker, K. H. Rubin, J. H. Haxel, and M. J. Fowler (2007), Rapid dike emplacement leads to dramatic hydrothermal plume release during seafloor spreading events, *Geology*, **35**, 579–582.
- Einarsson, P., and B. Brandsdóttir (1980), Seismological evidence for lateral magma intrusion during the July 1978 deflation of the Krafla Volcano in NE Iceland, *J. Geophys.*, **47**, 160–165.
- Embley, R. W., J. E. Lupton, G. Massoth, T. Urabe, V. Tunnicliffe, D. A. Butterfield, T. Shibata, O. Okano, M. Kinoshita, and K. Fujioka (1998), Geological, chemical, and biological evidence for recent volcanism at 17.5°S: East Pacific Rise, *Earth Planet. Sci. Lett.*, **163**, 131–147.
- Embley, R. W., W. W. Chadwick, M. R. Perfit, M. C. Smith, and J. R. Delaney (2000), Recent eruptions on the CoAxial segment of the Juan de Fuca Ridge: Implications for mid-ocean ridge accretion processes, *J. Geophys. Res.*, **105**, 16,501–16,525.
- Fouquet, Y., J. M. Auzende, V. Ballu, R. Batiza, D. Bideau, M. H. Cormier, P. Geistdoerfer, Y. Lagabriele, J. Sinton, and P. Spadea (1994), Variability of the present-day hydrothermal activity along an ultra-fast spreading ridge—East Pacific Rise between 17° and 19°S (Naudur Cruise), *C. R. Acad. Sci., Ser. II*, **319**, 1399–1406.
- Gauthier, P. J., and M. Condomines (1999), Pb-210–Ra-226 radioactive disequilibria in recent lavas and radon degassing: Inferences on the magma chamber dynamics at Stromboli and Merapi volcanoes, *Earth Planet. Sci. Lett.*, **172**, 111–126.
- Ghiorso, M. S., and R. O. Sack (1995), Chemical mass-transfer in magmatic processes, IV, A revised and internally consistent thermodynamic model for the interpolation and extrapolation of liquid-solid equilibria in magmatic systems at elevated temperatures and pressures, *Contrib. Mineral. Petrol.*, **119**, 197–212.
- Gill, J. B., and R. W. Williams (1990), Th-isotope and U-series studies of subduction-related volcanic rocks, *Geochim. Cosmochim. Acta*, **54**, 1427–1442.
- Hall, L. S., J. J. Mahoney, J. M. Sinton, and R. A. Duncan (2006), Spatial and temporal distribution of a C-like asthenospheric component in the Rano Rahi Seamount Field, East Pacific Rise, 15°–19°S, *Geochem. Geophys. Geosyst.*, **7**, Q03009, doi:10.1029/2005GC000994.
- Hart, S. R., and T. Dunn (1993), Experimental cpx melt partitioning of 24 trace-elements, *Contrib. Mineral. Petrol.*, **113**, 1–8.
- Haymon, R. M., et al. (1993), Volcanic eruption of the mid-ocean ridge along the East Pacific Rise crest at 9°45'–52°N: Direct submersible observations of sea-floor phenomena associated with an eruption event in April, 1991, *Earth Planet. Sci. Lett.*, **119**, 85–101.
- Hobson, J. M., R. M. Haymon, S. M. White, S. R. Baron, P. J. Sharfstein, K. C. Macdonald, D. Wright, and D. Scheirer (1997), Hydrothermal vents along the Spike segment of the southern EPR (17°15'–40°S), *Eos Trans. AGU*, **78**(46), Fall Meet. Suppl., F690.
- Hooft, E. E., and R. S. Detrick (1993), The role of density in the accumulation of basaltic melts at mid-ocean ridges, *Geophys. Res. Lett.*, **20**, 423–426.
- Hooft, E. E. E., R. S. Detrick, and G. M. Kent (1997), Seismic structure and indicators of magma budget along the southern East Pacific Rise, *J. Geophys. Res.*, **102**, 27,319–27,340.
- Jackson, A., A. R. T. Jonkers, and M. R. Walker (2000), Four centuries of geomagnetic secular variation from historical records, *Philos. Trans. R. Soc. London, Ser. A*, **358**, 957–990.
- Kent, D. V., and J. Gee (1996), Magnetic alteration of zero-age oceanic basalt, *Geology*, **24**, 703–706.
- Knight, M. D., and G. P. L. Walker (1988), Magma flow directions in dikes of the Koolau Complex, Oahu, determined from magnetic fabric studies, *J. Geophys. Res.*, **93**, 4301–4319.
- Koyanagi, R. Y., B. Chouet, and K. Aki (1987), Origin of volcanic tremor in Hawaii, *U.S. Geol. Surv. Prof. Pap.*, **1350**, 1221–1257.
- Kurz, M. D., M. Moreira, J. Curtice, D. E. Lott, J. J. Mahoney, and J. M. Sinton (2005), Correlated helium, neon, and melt production on the super-fast spreading East Pacific Rise near 17°S, *Earth Planet. Sci. Lett.*, **232**, 125–142.
- Macdonald, K. C. (1998), Linkages between faulting, volcanism, hydrothermal activity and segmentation on fast-spreading centers, in *Faulting and Magmatism at Mid-Ocean Ridges*, *Geophys. Monogr. Ser.*, vol. 106, edited by W. R. Buck et al., pp. 27–58, AGU, Washington, D. C.
- Mahoney, J., A. P. Le Roex, Z. Peng, R. L. Fisher, and J. H. Natland (1992), Southwestern limits of Indian Ocean Ridge mantle and the origin of low ²⁰⁶Pb/²⁰⁴Pb mid-ocean ridge basalt: Isotope systematics of the central Southwest Indian Ridge (17°–50°E), *J. Geophys. Res.*, **97**(B13), 19,771–19,790.
- Mahoney, J. J., J. M. Sinton, M. D. Kurz, J. D. Macdougall, K. J. Spencer, and G. W. Lugmair (1994), Isotope and trace-element characteristics of a super-fast spreading ridge: East Pacific Rise, 13–23°S, *Earth Planet. Sci. Lett.*, **121**, 173–193.
- McKenzie, D., and R. K. O'Nions (1991), Partial melt distributions from inversion of rare-earth element concentrations, *J. Petrol.*, **32**, 1021–1091.

- Mejia, V., N. D. Opdyke, and M. R. Perfit (1996), Paleomagnetic field intensity recorded in submarine basaltic glass from the East Pacific Rise, the last 69 Ka, *Geophys. Res. Lett.*, **23**(5), 475–478.
- Naar, D. F., and R. N. Hey (1989), Recent Pacific-Easter-Nazca plate motions, in *Evolution of Mid-Ocean Ridges*, *Geophys. Monogr. Ser.*, vol. 57, edited by J. M. Sinton, pp. 9–30, AGU, Washington, D. C.
- Nikogosian, I. K., and A. V. Sobolev (1997), Ion-microprobe analysis of melt inclusions in olivine: Experience in estimating the olivine-melt partition coefficients of trace elements, *Geochem. Int.*, **35**, 119–126.
- Niu, Y., D. Guy Waggoner, J. M. Sinton, and J. J. Mahoney (1996), Mantle source heterogeneity and melting processes beneath seafloor spreading centers: The East Pacific Rise, 18°–19°S, *J. Geophys. Res.*, **101**(B12), 27,711–27,734.
- Norrish, K., and J. T. Hutton (1969), An accurate x-ray spectrographic method for the analysis of a wide range of geological samples, *Geochim. Cosmochim. Acta*, **33**, 431–441.
- Oversby, V. M., and P. W. Gast (1968), Lead isotope compositions and uranium decay series disequilibrium in recent volcanic rocks, *Earth Planet. Sci. Lett.*, **5**, 199–206.
- Perfit, M. R., and W. W. Chadwick, Jr. (1998), Magmatism at mid-ocean ridges: Constraints from volcanological and geochemical investigations, in *Faulting and Magmatism at Mid-Ocean Ridges*, *Geophys. Monogr. Ser.*, vol. 106, edited by W. R. Buck et al., pp. 59–115, AGU, Washington, D. C.
- Pick, T., and L. Tauxe (1993), Holocene paleointensities: Thellier experiments on submarine basaltic glass from the East Pacific Rise, *J. Geophys. Res.*, **98**, 17,949–17,964.
- Renard, V., R. Hekinian, J. Francheteau, R. D. Ballard, and H. Backer (1985), Submersible observations at the axis of the ultrafast-spreading East Pacific Rise (17°–21°30'S), *Earth Planet. Sci. Lett.*, **75**, 339–353.
- Rochette, P., L. Jenatton, C. Dupuy, F. Boudier, and I. Reuber (1991), Diabase dike emplacement in the Oman Ophiolite: A magnetic fabric study with reference to geochemistry, in *Ophiolite Genesis and Evolution of the Oceanic Lithosphere*, edited by Tj. Peters et al., pp. 55–82, Minist. of Pet. and Miner., Muscat, Sultanate of Oman.
- Roeder, P. L., and R. F. Emslie (1970), Olivine-liquid equilibrium, *Contrib. Mineral. Petrol.*, **29**, 275–289.
- Rubin, A. M. (1993), Tensile fracture of rock at high confining pressure: Implications for dike propagation, *J. Geophys. Res.*, **98**, 15,919–15,935.
- Rubin, A. M., and D. D. Pollard (1987), Origins of blade-like dikes in volcanic rift zones, *U.S. Geol. Surv. Prof. Pap.*, **1350**, 1449–1470.
- Rubin, K. H., and J. D. Macdougall (1989), Submarine magma degassing and explosive magmatism at Macdonald (Tamarii) Seamount, *Nature*, **341**, 50–52.
- Rubin, K. H., and J. M. Sinton (2007), Inferences on mid-ocean ridge thermal and magmatic structure from MORB compositions, *Earth Planet. Sci. Lett.*, **260**, 257–276.
- Rubin, K. H., G. E. Wheller, M. O. Tanzer, J. D. Macdougall, R. Varne, and R. Finkel (1989), U-238 decay series systematics of young lavas from Batur Volcano, Sunda Arc, *J. Volcanol. Geotherm. Res.*, **38**, 215–226.
- Rubin, K. H., J. D. Macdougall, and M. R. Perfit (1994), ²¹⁰Po-²¹⁰Pb dating of recent volcanic eruptions on the sea floor, *Nature*, **368**, 841–844.
- Rubin, K. H., I. van der Zander, M. C. Smith, and E. C. Bergmanis (2005), Minimum speed limit for ocean ridge magmatism from Pb-210–Ra-226–Th-230 disequilibria, *Nature*, **437**, 534–538.
- Sæmundsson, K. (1991), Jarðfræði Kröflukerfisins, in *The Nature of Lake Mývatn*, edited by A. Gardarson and Á. Einarsson, pp. 2–95, Icelandic Natl. Sci. Soc., Reykjavik.
- Scheirer, D. S., and K. C. Macdonald (1993), Variation in cross-sectional area of the axial ridge along the East Pacific Rise: Evidence for the magmatic budget of a fast spreading center, *J. Geophys. Res.*, **98**, 7871–7885.
- Scheirer, D. S., K. C. Macdonald, D. W. Forsyth, and Y. Shen (1996), Abundant seamounts of the Rano Rahi seamount field near the southern East Pacific Rise, 15° to 19°S, *Mar. Geophys. Res.*, **18**, 13–52.
- Sigmarsson, O. (1996), Short magma chamber residence time at an Icelandic volcano inferred from U-series disequilibria, *Nature*, **382**, 440–442.
- Sigurdsson, H. (1987), Dyke injection in Iceland: A review, in *Mafic Dyke Swarms*, edited by H. C. Halls and W. F. Fahrigh, *Geol. Assoc. Can. Spec. Pap.*, **34**, 55–64.
- Sigurdsson, H., and S. R. J. Sparks (1978), Lateral magma flow within rifted Icelandic crust, *Nature*, **274**, 126–130.
- Sinton, J., E. Bergmanis, K. Rubin, R. Batiza, T. K. P. Gregg, K. Grönvold, K. C. Macdonald, and S. M. White (2002), Volcanic eruptions on mid-ocean ridges: New evidence from the superfast spreading East Pacific Rise, 17°–19°S, *J. Geophys. Res.*, **107**(B6), 2115, doi:10.1029/2000JB000090.
- Sinton, J. M., and R. S. Detrick (1992), Mid-ocean ridge magma chambers, *J. Geophys. Res.*, **97**, 197–216.
- Sinton, J. M., S. M. Smaglik, J. J. Mahoney, and K. C. Macdonald (1991), Magmatic processes at superfast spreading mid-ocean ridges: Glass compositional variations along the East Pacific Rise 13°–23°S, *J. Geophys. Res.*, **96**, 6133–6155.
- Sparks, R. S. J., P. Meyer, and H. Sigurdsson (1980), Density variation amongst mid-ocean ridge basalts: Implications for magma mixing and the scarcity of primitive lavas, *Earth Planet. Sci. Lett.*, **46**, 419–430.
- Stakes, D. S., M. R. Perfit, M. A. Tivey, D. W. Caress, T. M. Ramirez, and N. Maher (2006), The Cleft revealed: Geological, magnetic, and morphologic evidence for construction of upper oceanic crust along the southern Juan de Fuca Ridge, *Geochem. Geophys. Geosyst.*, **7**, Q04003, doi:10.1029/2005GC001038.
- Staudigel, H., J. Gee, L. Tauxe, and R. J. Varga (1992), Shallow intrusive directions of sheeted dikes in the Troodos Ophiolite—Anisotropy of magnetic susceptibility and structural data, *Geology*, **20**, 841–844.
- Staudigel, H., et al. (1999), Geochemistry and intrusive directions in sheeted dikes in the Troodos ophiolite: Implications for mid-ocean ridge spreading centers, *Geochem. Geophys. Geosyst.*, **1**(1), doi:10.1029/1999GC000001.
- Stewart, M. A., J. A. Karson, and E. M. Klein (2005), Four-dimensional upper crustal construction at fast-spreading mid-ocean ridges: A perspective from an upper crustal cross-section at the Hess Deep Rift, *J. Volcanol. Geotherm. Res.*, **144**, 287–309.
- Stolper, E., and D. Walker (1980), Melt density and the average composition of basalt, *Contrib. Mineral. Petrol.*, **74**, 7–12.
- Todt, W., R. A. Cliff, A. Hanser, and A. W. Hofmann (1996), Evaluation of a ²⁰²Pb-²⁰⁵Pb double spike for high-precision lead isotope analysis, in *Earth Processes: Reading the Isotopic Code*, *Geophys. Monogr. Ser.*, vol. 95, edited by A. Basu and S. Hart, pp. 429–437, AGU, Washington, D. C.
- Tolstoy, M., et al. (2006), A sea-floor spreading event captured by seismometers, *Science*, **314**, 1920–1922, doi:10.1126/science.1133950.

- Tryggvason, E. (1984), Widening of the Krafla fissure swarm during the 1975–1981 volcano-tectonic episode, *Bull. Volcanol.*, *47*, 47–69.
- Tryggvason, E. (1986), Multiple magma reservoirs in a rift zone volcano: Ground deformation and magma transport during the September eruption of Krafla, Iceland, *J. Volcanol. Geotherm. Res.*, *28*, 1–44.
- Turner, S., S. Black, and K. Berlo (2004), Pb-210–Ra-226 and Ra-228–Th-232 systematics in young arc lavas: Implications for magma degassing and ascent rates, *Earth Planet. Sci. Lett.*, *227*, 1–16.
- Ulmer, P. (1989), The dependence of the Fe²⁺-Mg cation-partitioning between olivine and basaltic liquid on pressure, temperature and composition, *Contrib. Mineral. Petrol.*, *101*, 261–273.
- Urabe, T., et al. (1995), The effect of magmatic activity on hydrothermal venting along the superfast-spreading East Pacific Rise, *Science*, *269*, 1092–1095.
- Varga, R. J., J. S. Gee, H. Staudigel, and L. Tauxe (1998), Dike surface lineations as magma flow indicators within the sheeted dike complex of the Troodos Ophiolite, Cyprus, *J. Geophys. Res.*, *103*, 5241–5256.
- Villemant, B., H. Jaffrezic, J. L. Joron, and M. Treuil (1981), Distribution coefficients of major and trace elements—Fractional crystallization in the alkali basalt series of Chaîne-Des-Puys (Massif Central, France), *Geochim. Cosmochim. Acta*, *45*, 1997–2016.
- White, S. M., K. C. Macdonald, and R. M. Haymon (2000), Basaltic lava domes, lava lakes, and volcanic segmentation on the southern East Pacific Rise, *J. Geophys. Res.*, *105*, 23,519–23,536.